



Observing Single Atoms

Master thesis

of

Chien-Ju Lee

Work performed under the guidance of
Prof. Dr. Harald Weinfurter

München, November 2011

Erstgutachter: Prof. Dr. G. Rempe
Zweitgutachter: Prof. Dr. H. Weinfurter

Contents

1. Introduction	1
2. Overview of the existing experiment	4
2.1. Rubidium 87	4
2.2. Trapping single atoms	6
2.3. Generation and verification of atom-photon entanglement	8
2.4. Implementing a fast atomic state detection scheme	10
3. Principles of laser cooling and trapping	12
3.1. Laser cooling	12
3.1.1. The radiation force	12
3.1.2. Optical molasses	13
3.1.3. Limits of laser cooling	14
3.2. Principle of magneto-optical traps	15
3.3. Optical dipole traps	16
3.3.1. The optical dipole force	17
3.3.2. A focused beam trap for ^{87}Rb	18
3.4. Summary	19
4. Magneto-optical trap	21
4.1. Magnetic coils	21
4.1.1. Quadrupole coils	21
4.1.2. Compensation coils	23
4.2. Preparation of the MOT beams	23
4.2.1. Cooling and repump laser systems	24
4.2.2. Optics for six arms splitting	24
4.3. Summary	27
5. Single atom trap	29
5.1. Dipole trap laser	29
5.1.1. Preparation of the trap beam	30
5.2. Confocal microscope	31
5.2.1. Dichroic mirrors	33
5.2.2. Optical alignment	34

5.2.3. Overlapping the foci of the beams	37
5.3. Summary and discussion	39
6. Summary and outlook	40
A. Appendix	42
A.1. Density matrix and optical Bloch equations	42
A.2. Equations for magnetic coils design	43
A.2.1. Quadrupole coils	44
A.2.2. Compensation coils	45
A.3. Experimental setup	46

1. Introduction

In 1935 Einstein, Podolsky and Rosen raised the question regarding the completeness of quantum mechanics, the so-called EPR-paradox, in their famous publication [1]. By assuming reality, locality and completeness, which according to them are essential properties of any physical theory, they proposed a gedankenexperiment leading to results contradicting quantum theory. This argumentation inspired the idea to extend quantum theory by adding local hidden variables (LHV), which are inaccessible in experiment but predetermine the outcomes of measurements on quantum systems. With this extension the quantum theory would become local, realistic and deterministic. However, the thought experiment in EPR-paradox was based on non-classical correlations of the position and momentum degrees of freedom of two particles, and the realization of such experiment was beyond the reach of experimental technology at that time. To realize such an experiment seemed impossible until Bohm proposed a simplified but equivalent version using two entangled spin-1/2 particles [2].

In 1964, based on Bohm's proposal, John Bell constructed an inequality, which allowed for the first time to distinguish quantum mechanics from any LHV theory, known as Bell's inequality [3]. In the following decades, many experiments have been done [4, 5, 6] yielding results in favor of quantum mechanics. However, all these experiments were subject to two so-called loopholes. One of them, known as the locality loophole, addresses the possibility of remote interaction between the measurement apparatuses or the entangled particles, and is closed by an experiment performed with entangled photons under strict relativistic locality conditions [7]. But due to the low detection efficiency of single photons, this experiment left open the detection loophole which describes the possibility that even if the detected particles behave according to quantum mechanics the whole ensemble does not. This detection loophole was closed in experiments with two neighboring entangled ions in a trap with high detection efficiency [8, 9], however, here the locality condition was not satisfied due to small spatial separation. Until today no experiment has managed to close both loopholes at the same time. One possible experimental scheme to achieve this goal is based on correlation measurements on two spin-entangled atoms at remote locations. Starting from entangling each of the atoms with a photon, a Bell-state measurement on the photons serves to swap the entanglement to the atoms [10, 11]. In such a scheme, the photons can be distributed far enough to ensure space-like separation while the high atomic detection efficiency can close the

detection loophole.

To realize such an experiment is the goal of our group. Being the key ingredient to perform a loophole-free Bell test, atom-photon entanglement has been demonstrated with single optically trapped ^{87}Rb atoms [12]. Moreover, it was also demonstrated that entanglement between the atom photon pair can be distributed over long distances. This is done by sending the photon through a 300 m long optical fiber and adopting a method to actively stabilize its polarization state [13, 14]. Two independent atom traps have been set up in separate locations [15, 16, 17]. Estimations based on current achievements have been done showing the feasibility of performing a loophole-free Bell test with given experimental parameters [18]. However, various improvements have been implemented since the first trap was constructed. The most significant one is a new method developed to detect the atomic state of single optically trapped atoms by laser ionization and the subsequent detection of the ionized fragments using channel electron multipliers (CEMs) [19]. To incorporate this new atomic state analysis method into current experimental scheme is the main motivation for constructing a new trap providing following advantages.

- By ionizing the trapped atoms, their atomic states projection can be done faster compared to the currently used scheme (resonant scattering of light, see sec. 2.3 for details). Integrating an ionization laser into the setup also opens possibilities to further improve the atomic state detection scheme.
- It has been demonstrated in our group that the CEMs can detect the ionization fragments with about 400 ns with high efficiency. Together with the ionization process, an overall detection time of the atomic state within 1 μs can be achieved. This will enable us to perform a direct loophole-free Bell test with two entangled atoms separated by 300 m.
- A microscope objective with a larger numerical aperture shall be used to increase the collection efficiency of photons from the trap region.

Overview

The structure of this thesis is as follows. First, an introduction to the experiment of atom-photon entanglement is presented. This includes a brief overview of the properties of ^{87}Rb , the atomic species used in our experiment, the idea of trapping a single ^{87}Rb atom with the combination of a magneto-optical trap and an optical dipole trap and the generation and verification of the entanglement. The third chapter introduces the physical principle of laser cooling and trapping, in particular the magneto-optical trap and the optical dipole trap. A magneto-optical trap (MOT) is used to prepare a small cloud of cold atoms which is used for loading the dipole trap. Chapter 4 describes the construction of a MOT, this includes the design of the magnetic coils and preparation of the six cooling beams. The last chapter is devoted to constructing a single-atom optical dipole trap. In a so-called confocal microscope,

the dipole trap laser and the ionization laser are focused to a small spot and precisely overlapped with the effective region of collection optics. Such an arrangement allows to trap single neutral ^{87}Rb atoms and provides a high collection efficiency for emitted photons.

2. Overview of the existing experiment

As mentioned in the introduction, the long term goal of our group is to perform a loophole-free Bell test. In order to fulfill this goal, two single atom traps utilizing the same principle for generating atom-photon entanglement had been set up in our lab. However, the integration of the newly developed photoionization technique, which enables faster detection of atomic states, requires to reconstruct the vacuum system of the first trap. Together with other difficulties, implementing the new atomic state detection scheme into the first trap is almost impossible (details will be discussed in the last section). Constructing a new single atom trap is thus a more practical solution. Since the mission of such a single atom trap is providing a suitable condition for generating entangled atom-photon pairs, the relevant knowledge accumulated in our group provides guidance for this work. The first two sections give an overview of how our single atom trap is operated - the level scheme of ^{87}Rb is first discussed, then the combination of a magneto-optical trap and an optical dipole trap to isolate single atoms is presented. In the third section the generation and verification of atom-photon entanglement is briefly summarized - both the physical principle and the experimental realization. Presenting the considerations from both the existing experiment and the new technique which affect the construction of the new trap is the main purpose of this chapter.

2.1. Rubidium 87

The atomic species used in our experiment is ^{87}Rb - an alkali atom with one valence electron and nuclear spin $I=3/2$. One of the reasons that alkali atoms are popular for laser cooling and trapping experiments, is because of their relatively simple level structure and the easy access of the transition frequencies from ground state to first excited states. In the case of ^{87}Rb , they are the 795 nm D_1 and the 780 nm D_2 lines (see fig: 2.1) lying in the near-infrared range which can be easily addressed by diode lasers. Since the inner electrons of an alkali atom form a closed shell, the only contribution to the total angular momentum of the atom comes from the valence electron; the total orbital and spin angular momentum of the atom, L and S respectively, are just that of the electron. The two momenta couple in the

usual way to form the total angular momentum of the atom:

$$|L - S| \leq J \leq L + S.$$

The lowest energy state of ^{87}Rb is $5^2S_{1/2}$, whereas the first excited states are $5^2P_{1/2}$ and $5^2P_{3/2}$. The splitting of the first excited state comes from the spin-orbit interaction, $\vec{L} \cdot \vec{S}$ which depends on the respective orientation of the two vectors.

Inclusion of the interaction between the nuclear spin \vec{I} with the total angular momentum of the atom \vec{J} leads to further splitting of states - the hyperfine splitting. The grand total angular momentum $\vec{F} = \vec{I} + \vec{J}$ is added up in the usual way and lies in the range:

$$|I - J| \leq F \leq I + J.$$

The interaction term $\vec{I} \cdot \vec{J}$ is the cause of the hyperfine splitting. For the ground state $5^2S_{1/2}$ with $J=1/2$, this results in the splitting in $F = 1$ and $F = 2$ hyperfine levels, each of them consisting of 3 and 5 Zeeman substates respectively. Figure 2.1 shows the detailed structure of the ground state and the lowest lying P states of ^{87}Rb atoms. A notation is adopted when referring to a specific Zeeman state: the symbol $|F, m_F\rangle$ stands for those in the ground hyperfine states and $|F', m'_{F'}\rangle$ for the excited ones.

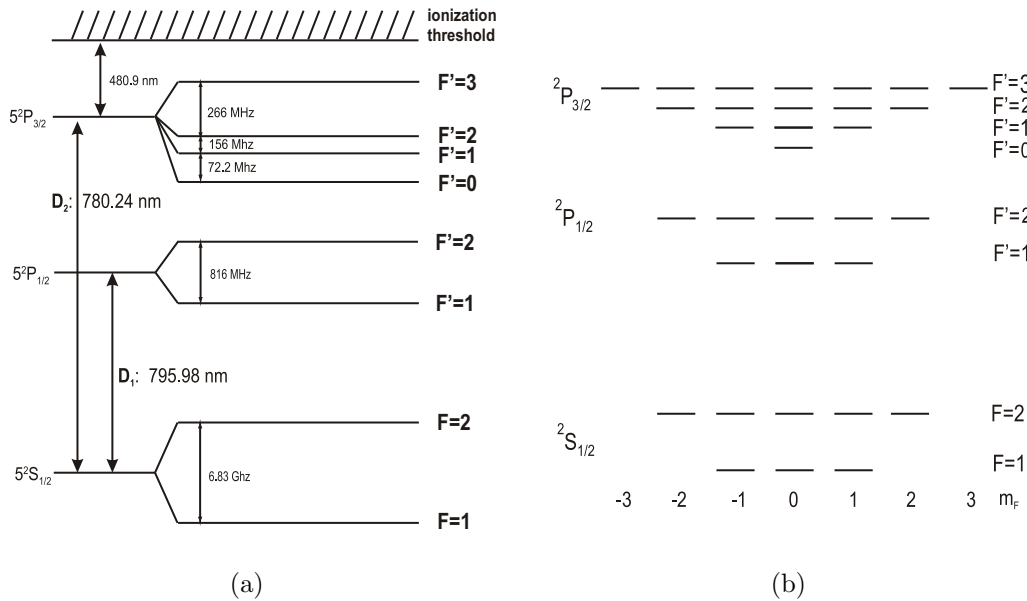


Figure 2.1.: Level scheme of ^{87}Rb . a) Hyperfine structure of the ground $5^2S_{1/2}$ and the first two excited levels $5^2P_{1/2}$ and $5^2P_{3/2}$ and the relevant transition lines. b) The corresponding Zeeman states.

2.2. Trapping single atoms

For experiments with single atoms, in particular atom-photon entanglement, one has to trap a single atom at a localized position and isolate it from the environment. Three kinds of traps for neutral atoms can be realized via different kinds of forces: magneto-optical traps, magnetic traps and optical dipole traps. However, merely trapping single atoms is not sufficient to generate the atom-photon entanglement and further conditions have to be fulfilled. The first requirement comes from the need to prepare and analyze internal atomic states. This excludes the use of a magneto-optical trap, which relies on dissipative forces from light scattering, and consequently does not preserve the internal atomic state. The magnetic trap is also improper for our purpose, because it is based on the state-dependent force on the magnetic dipole momentum in a magnetic field gradient. Since the direction of the resultant force depends on the orientation of the magnetic dipole moment of the atom relative to the external magnetic field, it is not possible to trap all internal states which are used in the atom-photon entanglement. The only candidate left which satisfies all the requirements mentioned above is the optical dipole trap. The trapping mechanism of an optical dipole trap relies on the interaction of an incident light beam with the induced electric dipole moment of the atom. For far red-detuned linearly polarized light, the optical excitation can be kept extremely low and the trapping potential is independent of the ground state hyperfine and Zeeman structure.

Loading single atoms

An optical dipole trap provides only a conservative force with typical trap depths in the range around one mK. This trapping potential is too shallow to capture atoms in a gas at room temperature. In order to load atoms into the optical dipole trap cold atoms with energy well below the depth of the dipole trap must be prepared first. A magneto-optical trap (MOT) is set up to trap an ensemble of atoms which are cooled to the micro-Kelvin regime [20] before being loaded into the dipole trap. More details about MOT can be found in chapter 4.

To load atoms into the dipole trap the magneto-optical trap and the optical dipole trap must operate simultaneously. The center point of the MOT is adjusted to coincide with the focus of the dipole trap beam. During the loading process the MOT provides a high density of cold atoms and a friction force (from cooling laser) which allows the atoms to be captured in the conservative dipole potential. An important feature of the dipole trap used in our lab is that it is strongly focused. With such configuration a blockade mechanism occurs and prevents the atom number inside the trap to be more than one [21]. This mechanism provides us a convenient way to ensure that only one atom at a time is stored in the trap without making additional effort. For a focused beam trap this effect can be observed for beam waists below 4

μm [15].

Vacuum chamber

The trapping time of atoms in the dipole trap is limited mainly by collisions with the background gas. In order to achieve a long storage time, the experiment must be carried out under an ultra-high vacuum condition. A spectroscopy glass cell which provides good optical access is attached to the vacuum chamber. A Rubidium dispenser inside the UHV chamber operating under a steady DC current serves as the atom source. After being evacuated by a turbo pump, the vacuum of the chamber is maintained by an ion-getter pump and yields a background pressure below 10^{-11} mbar and the residual Rb gas pressure below 10^{-10} mbar. This enables storage times of atoms in the dipole trap of several seconds [15, 17].

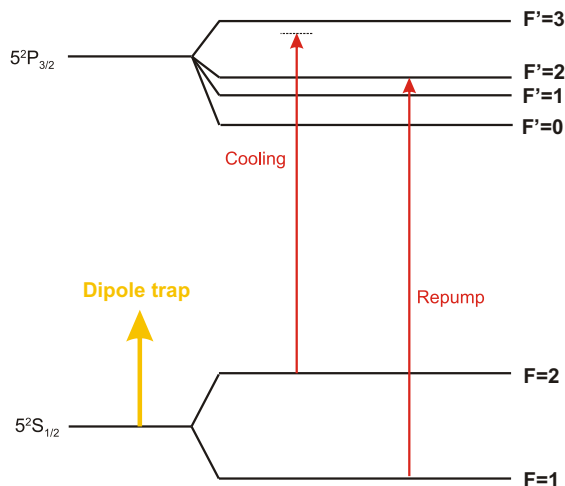


Figure 2.2.: Three laser frequencies involved for cooling and trapping single atoms.

Laser system

Three lasers are involved in trapping single atoms. Two of them are used to generate the six laser beams used in the MOT and the other is used to generate the dipole trap. The cooling laser which is red-detuned from the atomic transition $5^2S_{1/2}$, $F = 2 \rightarrow 5^2P_{3/2}$, $F' = 3$ is used to provide the dissipative force during the cooling process. However, there is a finite probability that the excited atoms spontaneously decay to the $5^2S_{1/2}$, $F = 1$ ground state, and as a result are no more resonant to the cooling light. A separate repump laser which is resonant to the $5^2S_{1/2}$, $F = 1 \rightarrow 5^2P_{3/2}$, $F' = 2$ is therefore used to pump atoms back to the cooling cycle (see fig. 2.2). A 856 nm laser beam is used to generate the far off-resonance dipole trap, and is strongly focused by a microscope objective to ensure that the blockade mechanism

occurs and only one atom at a time is trapped.

2.3. Generation and verification of atom-photon entanglement

In our experiment, the spontaneous decay of an excited atom accompanied by the emission of a single photon is used to generate atom-photon entanglement. The atom is first prepared in the $|F' = 0, m'_F = 0\rangle$ state, which has a lifetime of 26 ns. From the excited state it decays spontaneously to the $F = 1$ ground state. There are three possible decay channels for this process which lead to different final atomic ground states - the $m_F = \pm 1, 0$ magnetic substates in this case, see fig. 2.3. Accompanying the decay of the excited atom a photon is emitted in one of the σ^\pm or π -polarization state. By defining a quantization axis - the optical axis of the microscope objective that collects the emitted photons in our case - the angular momentum of the atom and the photon can be determined with respect to this axis. With this definition, the projection of the photonic angular momentum on the quantization axis is $\pm\hbar$ for the σ^\pm -polarized photons and zero for π -polarized ones. Conservation of angular momentum determines the corresponding angular momenta carried by the emitted photon and the resultant ground state atom, see fig. 2.3. However, the π -photons are emitted perpendicularly to the quantization

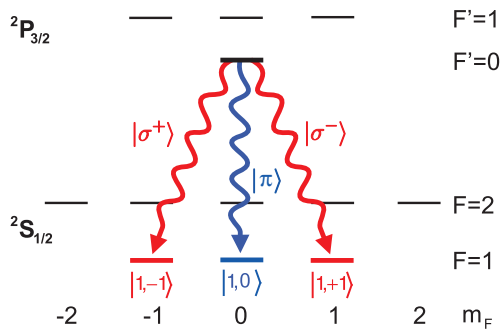


Figure 2.3.: Scheme of the spontaneous decay leading to entanglement. The atom is first excited to the $|F' = 0, m'_F = 0\rangle$ state which carries zero angular momentum with respect to the quantization axis. The conservation of angular momentum thus requires the momenta carried by the resultant atom photon pair also to sum up to zero.

axis, and the definition of the quantization axis along the collection optics exclude the possibility to observe photons emitted from the π -transition [16]. In the case of completely degenerate Zeeman substates both of the σ^\pm decay channels have the

same energy, and the final state of the atom-photon system can be written as

$$|\Psi\rangle = \frac{1}{\sqrt{2}}(|\sigma^+\rangle|1, -1\rangle + |\sigma^-\rangle|1, +1\rangle). \quad (2.1)$$

The experimental procedures of preparing the initial state for atom-photon entanglement and, its subsequent detection are summarized in the following [22, 23].

Preparation of the initial state

The atom is prepared in the initial ground state $|F = 1, m_F = 0\rangle$ by optical pumping. This is done by simultaneously applying two π -polarized pump beams which are resonant to the $F = 2 \rightarrow F' = 1$ and $F = 1 \rightarrow F' = 1$ transition of the D2 - line. Due to the presence of two dark states $|F = 2, m_F = \pm 2\rangle$ for the two pumping beams, the cooling beams of the MOT are additionally switched on in order to entirely empty the $F=2$ hyperfine state. The atom will end up being trapped in the $|F = 1, m_F = 0\rangle$ state, since under the applied laser configuration this state is only resonant to $|F' = 1, m'_F = 0\rangle$ state and such transition is forbidden by the selection rules. The duration of the optical pumping process is optimized to $2 \mu s$ [23].

A short π -polarized laser pulse is used to excite the prepared initial atomic state to the $|F' = 0, m'_F = 0\rangle$ state in $5^2P_{3/2}$. Subsequently, the spontaneous decay of the excited atom yields an entangled atom-photon pair as explained above.

Verification of atom-photon entanglement

The spontaneously emitted photon is collected by a microscope objective and coupled into a single mode fiber. The photon is then guided to an analyzer which consists of a polarizing beam splitter, a half-wave-plate and a quarterwave-plate and allows to perform a projective measurement in any basis.

Once a photon is detected, the sequence for the atomic state analysis will be started. The atomic state detection is a two-step process [16]. First, a selected superposition of the two Zeeman states $|1, -1\rangle$ and $|1, +1\rangle$ is transferred to the $F = 2$ level via a so-called STIRAP-technique leaving the orthogonal superposition in $F = 1$. A push-out laser then is applied and the atom will be removed from the trap if it is in the $F = 2$ level. Thereby the original Zeeman state of the atom can be inferred by verifying whether the atom was removed or not. To distinguish the two possible outcomes (atom in the trap or not), the cooling and repump lasers of the MOT are switched on and the fluorescence from the dipole trap region is sampled. For the second atom trap in our lab, the push-out process is replaced by a two-step state-selective photoionization method [17, 19].

2.4. Implementing a fast atomic state detection scheme

One of the obstacles to performing a loophole-free Bell test by means of our experimental scheme is the detection time of the atomic state. As mentioned above, the atomic state detection scheme used in our first trap relies on integrating the fluorescence photons from the trap region. A disadvantage of this method is the long duration for sampling these photons until the outcome can be determined, typically 10 to 20 ms [18]. A new detection method for a single optically trapped atoms has been demonstrated in our lab based on hyperfine-state-selective photoionization and subsequent registration of the correlated photoion-electron pairs by channel electron multipliers (CEM) [19]. The idea is that once the STIRAP process is finished during the atomic state detection, instead of pushing the atom out of the trap by scattering light on it, the atom is first excited to the $F'=3$ level and subsequently ionized by a blue laser. Two opposing CEMs are used to detect the produced ion-electron pair. With such a scheme the state analysis of atoms can be done in less than $1\mu\text{s}$ with an overall detection efficiency exceeding 98% [19].

It is also shown that the ionization probability is related to the photon flux of the ionization laser [24]. By using a 473 nm blue laser with 32.8 mW laser power and focused to $\omega=1.13\ \mu\text{m}$, an ionization probability of 0.99 is achieved after an ionization time of 386 ns.

However, to incorporate this new atomic state analysis scheme into the first trap without making significant changes is barely impossible. The reasons are summarized below.

- An arrangement called confocal microscope is used in our experimental scheme to overlap the trap region of the optical dipole trap (the focus of the dipole trap laser in our case) with the focus of the collection optics (details of confocal microscope see sec. 5.2). The ionization laser has to be integrated into the microscope and its focus overlapped with the other two beams in order to ionize trapped atoms with highest probability. The first trap has a completely different design of the confocal microscope, therefore a new one has to be built.
- Single atoms are trapped inside a glass cell connected to the vacuum system, thus the CEMs should be installed in the same glass cell. The one used in the old trap is too small to accommodate the CEMs. Because of the enlarged glass cell a new design for the magneto-optical trap is also needed. New vacuum system is required to integrate the CEMs. Since they operate under high voltages, additional component which allows the connection of the electrode to voltage source is needed.

- Taking the opportunity of constructing a new trap, a microscope objective with a larger numerical aperture (NA=0.5) can be used to replace the old one (NA=0.38) in order to increase the collection efficiency of the entangled photons.

Summary

Principles of the experimental scheme for atom-photon entanglement is presented in this chapter. The joint operation of a MOT and an optical dipole trap is the key point to successfully trap a single ^{87}Rb atom. Techniques of laser cooling and trapping are needed to carry out the construction work of a single atom trap. In the next chapter, the physics behind the techniques of laser manipulation of atoms is introduced. Afterward, two chapters are devoted to constructions of the MOT and the single atom trap, respectively.

3. Principles of laser cooling and trapping

The usage of lasers to manipulate and trap atoms has revolutionized the field of atomic physics, and opened up completely new research areas such as quantum information and computation. In 1975 the possibility of using lasers to cool atoms was proposed [25]. A decade later the first experimental observation of 3-D cooling [26] and optical trapping [27] of atoms are reported. Since the objective of this work is to construct a single atom trap which utilizes laser cooling and trapping techniques, the relevant physics is reviewed in this chapter.

3.1. Laser cooling

Although the concept of light pressure was familiar by physicists at the beginning of twentieth century, due to the low brightness of available light sources at that time, its mechanical effect was considered insignificant. However the invention of lasers changed the situation. Laser cooling techniques resides on the radiation force exerting on atoms by laser beams. In this section, the effect of light pressure on atoms and the principle of laser cooling technique will be presented.

3.1.1. The radiation force

The radiation force can be readily understood from the conservation of momentum when an object absorbs radiation. If an atom of mass m absorbs a photon of momentum $\hbar k$, the energy of the photon will be almost entirely converted to the internal energy of the atom, and the atom will end up in an excited state. The absorbed momentum will, however, accelerate the atom in the direction of the incoming light by the amount of $\frac{\hbar k}{m}$. Since the excited atom is unstable, it will decay back to the ground state through emitting a photon. When the atom decays through spontaneous emission, the random nature of such process will lead to an isotropic radiation distribution, the average change of the atomic momentum in such process is therefore zero. Also, if the atom decays through stimulated emission, since the emitted photon goes in the same direction as the incoming light, this process will not contribute to the change of the momentum. Therefore, scattering of photons

gives an average force in the direction of the incident light. This results in decreasing the velocity component of the atom in the direction opposing the propagating direction of the light beam. The magnitude of this force can be calculated by (photon momentum) \times (scattering rate) and written as

$$F_{scatt} = \hbar k \Gamma \rho_{ee} \quad (3.1)$$

where Γ and ρ_{ee} are the natural linewidth and the population in the excited state respectively. The fraction of the population in the excited state is given in eq. A.9, so that

$$F_{scatt} = \hbar k \frac{\Gamma}{2} \frac{\Omega^2/2}{\delta^2 + \Omega^2/2 + \Gamma^2/4} \quad (3.2)$$

The frequency detuning of the incoming photons from resonance taking into account the Doppler shift is $\delta = \omega - \omega_0 + \mathbf{k} \cdot \mathbf{v}$. The Rabi frequency Ω is related to the beam intensity by

$$\frac{I}{I_{sat}} = \frac{2\Omega^2}{\Gamma^2} \quad (3.3)$$

where $I_{sat} = \pi \hbar c / 3 \lambda^3 \tau$ is the saturation intensity and τ is the lifetime of the excited state. Inserting this relation into 3.2 one obtains

$$F_{scatt} = \hbar k \frac{\Gamma}{2} \frac{I/I_{sat}}{1 + I/I_{sat} + 4\delta^2/\Gamma^2}. \quad (3.4)$$

As one can see at high intensity of incident light this scattering force tends to a limiting value of $F_{max} = \hbar k \Gamma / 2$. This is because at high intensity the population of the upper and lower levels both approach 1/2.

3.1.2. Optical molasses

Free atoms move in all directions. In order to cool atoms in a vapor, we need laser cooling in three orthogonal directions. 'Optical molasses' is such a laser cooling technique that uses the configuration of three orthogonal sets of counter-propagating laser beams. These laser beams are derived from a single laser beam and have the same frequency. Each of the beams has approximately the same intensity as that of its counter-partner. We now focus on one-dimension case, for instance, considering an atom moving in the $+z$ direction. The force exerted by the counter-propagating beam pair with frequency detuning $\Delta = \omega - \omega_0$ on this atom is (see eq.3.4)

$$F_{\pm} = \pm \hbar k \frac{\Gamma}{2} \frac{I/I_{sat}}{1 + I/I_{sat} + [2(\Delta \mp kv)/\Gamma]^2} \quad (3.5)$$

3. Principles of laser cooling and trapping

Here the upper (lower) sign refers to the force from the laser beam propagating in the positive (negative) z direction. One can see that the radiation forces from this pair of counter-propagating beams only balance each other for a stationary atom. For a moving atom the Doppler shift will lead to different scattering rate of the two beams, therefore resulting in an imbalance in the forces. In the low intensity limit: $I/I_{sat} \ll 1$, the assumption that the two waves act independently on the atom can be adopted and the resultant force can be calculated by $F_+ + F_-$. In the approximation that $kv \ll \Gamma, |\Delta|$ we get [28]

$$F_{molasses} = 4\hbar k^2 \frac{I}{I_{sat}} \frac{(2\Delta/\Gamma)v}{[1 + (2\Delta/\Gamma)^2]^2} \quad (3.6)$$

The term I/I_{sat} in the denominator has been neglected by the low intensity limit. For red detuning, the light exerts a frictional, or damping, force on the atom and can be written as a product of a damping coefficient and the velocity:

$$F_{molasses} = -\alpha v \quad (3.7)$$

Because of the resemblance between this damping force and that experienced by a particle in a viscous fluid, both of which having the magnitude proportional to the velocity, this technique is given the name 'optical molasses' and was first demonstrated in 1985 [26].

3.1.3. Limits of laser cooling

If there is no other influence on the atomic motion besides the dissipative force, all atoms should decelerate to $v=0$ and reach $T=0$, which is an unphysical result. In reality, the cooling light beams also cause heating which is a result of the momentum diffusion due to the random direction of spontaneous emission. The competition between the heating and the damping force (of eq. 3.6) in optical molasses will result in a nonzero kinetic energy in steady state. This leads to the so-called Doppler cooling limit which gives a lower bound of the temperature that can be reached. This minimum temperature, also known as Doppler temperature, has the value [29]

$$T_D = \frac{\hbar\Gamma}{2k_B}, \quad (3.8)$$

where k_B is Boltzmann's constant and Γ the natural linewidth.

However, the Doppler cooling limit is derived under the assumption of non-degenerate two-level systems in the presence of a homogeneous radiation field. These assumption breaks down when counter-propagating beams with orthogonal polarization are used which produce inhomogeneous fields; and when the external magnetic field is compensated properly resulting in degenerate atomic states. It is shown both

experimentally [30] and theoretically [31] that the temperature of cold atoms in optical molasses can be much colder than the Doppler limit.

In our experiment the $\sigma^+ - \sigma^-$ laser configuration (see 3.2) is used for the MOT, also the external magnetic field is compensated (see sec. 4.1). As a result, the trapped ^{87}Rb atoms at temperature below the Doppler limit, about $105 \mu\text{K}$ (Doppler limit for ^{87}Rb is $146 \mu\text{K}$), are observed [15, 16].

3.2. Principle of magneto-optical traps

In the optical molasses, cold atoms accumulated in the intersection region of the three pairs of laser beams can still diffuse out. However, with the correct choice of the polarizations of the beams in addition to a magnetic field gradient this configuration can turn into a trap for cold atoms, the so-called magneto-optical trap [20].

The working principle of a MOT is using a pair of coils with currents in opposite direction to produce a magnetic quadrupole field centered at the intersection region of the laser beams. The field magnitude is zero at the center of the trap and increases linearly in every direction for small displacements from the center. As an atom moves in any direction from the zero point, this uniform field gradient shifts the atomic energy levels, in particular the Zeeman effect causes the energy of the three sub-levels of the $J=1$ level to vary linearly with the atom position, as shown for z -direction in Fig.3.1. The counter-propagating beams are circularly polarized with their frequency slightly tuned below the atomic resonance frequency. If an atom is at a position $z > 0$, the $\Delta M_J = -1$ transition will move closer to resonance leading to an increased absorption of photons from the σ^- beam. This will result in a restoring force pushing the atoms back to the trap center.

Consider an atom moving along z -axis toward positive direction. The restoring force of this atom at position z can be calculated by incorporating the frequency shift caused by the Zeeman effect into the frequency detuning δ used in eq.3.2 giving [32]:

$$\begin{aligned} F_{MOT} &= F_{scatt}^{\sigma^+}(\omega - kv - (\omega_0 + \beta z)) - F_{scatt}^{\sigma^-}(\omega + kv - (\omega_0 - \beta z)) \\ &\simeq -\alpha v - \frac{\alpha\beta}{k}z \end{aligned} \quad (3.9)$$

Where βz is the frequency shift due to Zeeman effect at the position z , and can be evaluated to be

$$\beta z = \frac{g_J \mu_B}{\hbar} \frac{\partial B}{\partial z} z, \quad (3.10)$$

where μ_B is the Bohr magneton and g_J the Landé g factor. As one can see in eq. 3.9 that, besides the damping force from the molasses (eq. 3.7), atoms in the MOT will experience a spatially dependent restoring force with coefficient $\alpha\beta/k$. This is the

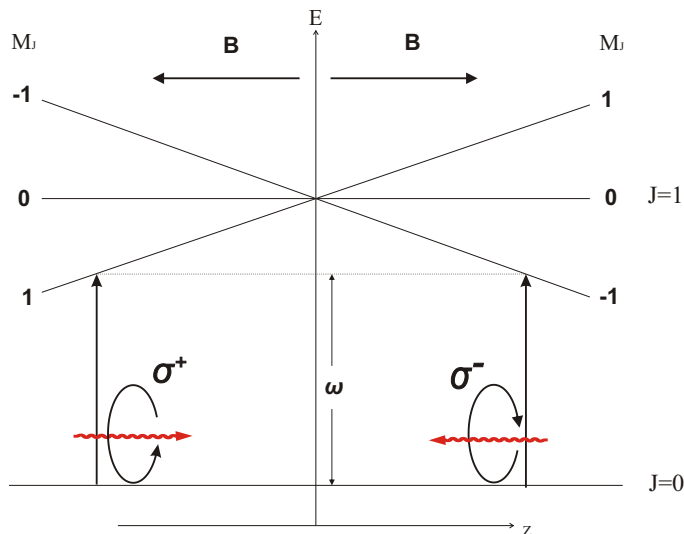


Figure 3.1.: Illustration of the mechanism for trapping atoms in a magneto-optical trap. Atoms with a $J=0$ to $J=1$ transition is placed in a linearly varying magnetic field. In the gradient field the Zeeman splitting of the sub-levels depend on the atoms position. The different Zeeman shift of the $M_J=\pm 1$ sub-levels and the selection rules for transitions between Zeeman states caused an imbalanced radiation force which will push the atoms back to the center of the trap.

force that traps atoms in the central region of a MOT. The further away an atom from the center of the trap the stronger the restoring force it will experience.

3.3. Optical dipole traps

In our experiment single ^{87}Rb atoms are stored in an optical dipole trap. From the classical point of view, the optical dipole force arises from the interaction of the induced electric dipole moment of atoms with the inhomogeneous driving electric field, in our case a focused Gaussian laser beam. In this section, a quantum mechanical approach following [33] is adopted to explain the physics of an optical dipole trap. Its purpose is to provide an intuitive way to understand the origin of the dipole force as well as to present the equations which will be used to estimate the performance of the trap, such as the trap depth for ^{87}Rb atoms, in chapter 5.

3.3.1. The optical dipole force

In quantum mechanical description, the dipole force experienced by atoms in a light field can be understood as a spatially varying ground-state potential caused by the intensity gradient of the light field. The origin of this potential is the energy level shift of an atom immersed in an oscillating electric field, and is known as AC-Stark shift or light shift in quantum mechanics.

In the case of an optical dipole trap, the effect of the far-detuned laser light on the atomic levels can be treated as a second order perturbation of the electric field. For non-degenerate atomic states, the energy shift of the i -th state caused by an interaction Hamiltonian H_{int} in time-independent perturbation theory is given by

$$\Delta E_i = \sum_{j \neq i} \frac{|\langle j | H_{int} | i \rangle|^2}{\varepsilon_i - \varepsilon_j}, \quad (3.11)$$

where ε_i are the energy of the unperturbed states. The interaction Hamiltonian is $H_{int} = -\hat{\mu} \hat{\mathbf{E}}$, where $\hat{\mu} = -e\mathbf{r}$ represents the electric dipole operator. Consider the combined atom-photon system in the dressed state picture. An atom in the ground state $|i\rangle$ with the light field consisting of n photons with frequency ω will have the unperturbed energy of $\varepsilon_i = n\hbar\omega$. On the other hand, when the atom is excited to a state $|j\rangle$ with energy $\hbar\omega_j$ higher than $|i\rangle$ by absorbing a photon, the unperturbed energy of the system will become $\varepsilon_j = \hbar\omega_j + (n-1)\hbar\omega = -\hbar\Delta_{ij} + n\hbar\omega$ with $\Delta_{ij} = \omega - \omega_j$ being the detuning of the light field relative to the atomic transition which is considered. For a two-level atom (see fig. 3.2(a)) with energy difference $\hbar\omega_0$, equation (3.11) reduces to

$$\Delta E = \pm \frac{|\langle e | \mu | g \rangle|^2}{\hbar\Delta} |E|^2 = \pm \frac{3\pi c^2 \Gamma}{2\omega_0^3 \Delta} I, \quad (3.12)$$

with plus and minus sign corresponding to the shift of ground and excited state respectively.

In the interesting case of low saturation, the atom spends most of the time in the ground state and the light shift of the ground state can be interpreted as the relevant mechanical potential. Also one can see from 3.12 that the optically induced energy shift depends on the field intensity. Therefore, an atom in an red-detuned (blue-detuned) inhomogeneous light field will experience an attractive (repulsive) conservative force with magnitude equal to the gradient of the light shift toward the intensity maximum, see fig. 3.2(b).

It can be shown that an important relation between the scattering rate and the dipole potential exists [33]:

$$\hbar\Gamma_{sc} = \frac{\Gamma}{\Delta} U_{dip}, \quad (3.13)$$

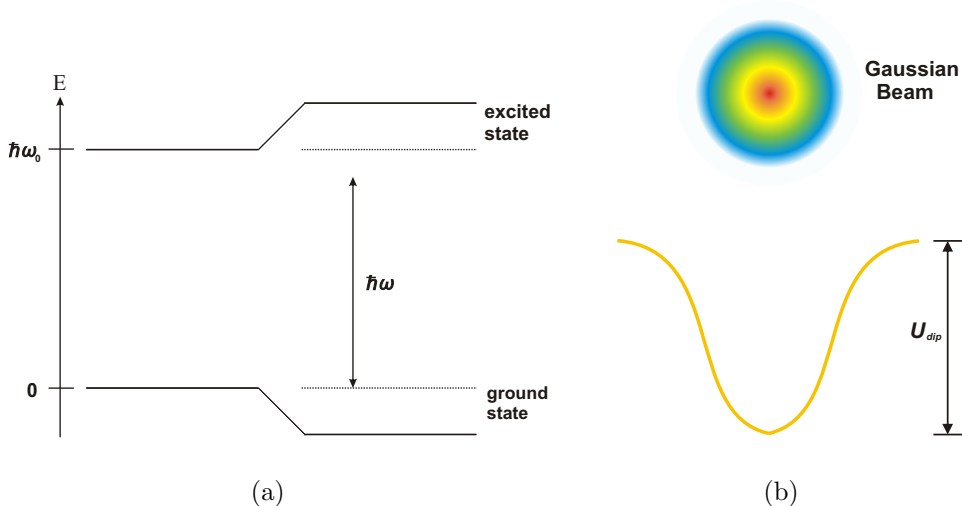


Figure 3.2.: a) Light shifts of a two-level atom induced by a red-detuned light field. While the ground state is lowered, the excited state is shifted upward by the same amount. b) The trapping potential U_{dip} generated by a red-detuned Gaussian laser beam, where the lowest point of the potential is at the intensity maximum of the beam.

where U_{dip} is the induced light shift given by 3.12. From eq. 3.12 and 3.13 one can see that the dipole potential scales as I/Δ , whereas the scattering rate scales as I/Δ^2 . This is the reason a far-detuned laser beam is usually used to generate the dipole trap, to keep the scattering rate as low as possible.

3.3.2. A focused beam trap for ^{87}Rb

In real atoms used for atom trapping experiments, e.g. ^{87}Rb for our experiment, the electronic transition has a complex sub-structure. The main consequence is that the dipole potential in general depends on the particular sub-state of the atom. However, as long as the optical detunings stay large compared with the excited-state hyperfine splitting, it is reasonable to assume those splittings are unresolved. With this assumption a general result of the dipole potential for the ground state $5^2S_{1/2}$ can be derived [33]:

$$U_{dip}(\mathbf{r}) = \frac{\pi c^2 \Gamma}{2\omega_0^3} \left(\frac{2 + \wp g_F m_F}{\Delta_{2,F}} + \frac{1 - \wp g_F m_F}{\Delta_{1,F}} \right) I(\mathbf{r}), \quad (3.14)$$

where g_F is the atomic Landé factor, and $\wp = 0, \pm 1$ for π - and σ^\pm -polarized light. The detunings of the light field $\Delta_{1,F}$ and $\Delta_{2,F}$ refer to the D_1 and D_2 lines respectively, and the factor Γ/ω_0^3 is the same for both lines. In our experiment, the dipole trap is generated by a linearly polarized laser beam with wavelength $\lambda = 856$ nm which is red detuned 76 nm and 61 nm from the D_2 and D_1 line respectively. By creating a strongly focused Gaussian beam, the atoms immersed in the light field will experience maximal light shift at the focus, thus a three dimensional potential well for the atoms is created. The intensity profile of a Gaussian laser beam propagating in the z -direction is

$$I(r, z) = \frac{2P}{\pi w^2(z)} e^{-\frac{2r^2}{w^2(z)}}, \quad (3.15)$$

where P is the power of the beam and r the distance from the optical axis. The $1/e^2$ -radius $w(z)$ of a Gaussian laser beam is given by

$$w(z) = w_0 \sqrt{1 + \left(\frac{z}{z_R}\right)^2} \quad (3.16)$$

with $z_R = \pi w_0^2/\lambda$ the Rayleigh length and w_0 the beam waist. The maximum intensity of a Gaussian beam is given by $2P/(\pi w_0^2)$. Single atoms will be trapped in an ellipsoidal region centered at the beam focus. The potential can be approximated near the center of the beam by the harmonic potential

$$U(r, z) \approx -U_0 \left[1 - 2 \left(\frac{r}{w_0}\right)^2 - \left(\frac{z}{z_R}\right)^2 \right]. \quad (3.17)$$

The maximum trap depth U_0 for a ^{87}Rb atom under our experimental conditions following 3.14 is

$$U_0 = \frac{c^2 \Gamma}{\omega_0^3 w_0^2} \left(\frac{2}{\Delta_{D_2}} + \frac{1}{\Delta_{D_1}} \right) P \quad (3.18)$$

The corresponding radial and axial trap frequencies are given by

$$w_r = \sqrt{\frac{4U_0}{mw_0^2}} \quad \text{and} \quad w_z = \sqrt{\frac{2U_0}{mz_R^2}}. \quad (3.19)$$

3.4. Summary

Principles of laser cooling and trapping which are relevant to this work is discussed in this chapter. Three pairs of counter-propagating laser beams along three spatial axes can be used to decelerate atoms in all directions and leads to cooling in three-dimension. This so-called optical molasses is used in our scheme to cool ^{87}Rb atoms

3. Principles of laser cooling and trapping

to around a hundred μK . Used together with quadrupole coils generating magnetic field gradient, this configuration can turn into a trap for neutral atoms. As one can imagine, since the trapping force of a MOT is proportional to the field gradient, see eq. (3.9) and (3.10), the atomic density in the trap region changes according to the applied field gradient. In the next chapter the experimental realization of a magneto-optical trap is treated in detail. On the other hand, the origin of optical dipole forces can be understood as the mechanical potential of atoms caused by an inhomogeneous light field. To derive the relevant potential for ^{87}Rb , the complexity can be reduced by assuming that the hyperfine structures are unresolved as long as the optical detuning is large. Once the single atom trap is complete, its trap depth for ^{87}Rb can be calculated by inserting the estimated available power and the beam waist of the trap beam in eq. (3.18).

4. Magneto-optical trap

In our experimental scheme the magneto-optical trap is used to prepare a localized high density cloud of cold atoms to be loaded into the single atom trap. As explained in chapter 3, a MOT is an arrangement consisting of three pairs of counter propagating cooling beams and a magnetic field gradient. The field gradient is generated by a coil-pair, and its magnitude at the trap region will determine the strength of the confinement. To achieve the desired field gradient under a few Amperes current supply without causing heating problem of the coils is important, and the design of it is treated in detail in the first section. On the other hand, in order to generate the orthogonal $\sigma^+ - \sigma^-$ counter-propagating cooling beams which are also essential for the trapping mechanism to occur, polarization-maintaining fibers are used to guide each of them to the MOT. Starting from the laser systems the optical preparation of the MOT beams is presented in the second section.

4.1. Magnetic coils

Two kinds of magnetic coils are used in the experiment: the quadrupole coils used to create the magnetic field gradient and the compensation coils used to generate uniform magnetic field. The magnetic field gradient is essential to trap neutral atoms as explained in section 3.2. The compensation coils are used to offset external magnetic fields such that the magnetic field at the region where single atoms are trapped is zero. This is critical for atom-photon entanglement in our experimental scheme. Since in our case the atomic qubit is stored in Zeeman states of $F=1$ hyperfine ground level, they are susceptible to magnetic fields due to their magnetic moment. Under the influence of external magnetic fields these Zeeman states will undergo undesired evolution and energy splitting between each other, as a result the fidelity of atom-photon entanglement can be reduced. The compensation coils is one of the crucial elements of a method developed to actively control the magnetic field at the trap region [22].

4.1.1. Quadrupole coils

Two coils arranged in anti-Helmholtz configuration are used to generate the magnetic quadrupole field, fig. 5.6(a). A mechanical frame is designed for sustaining the

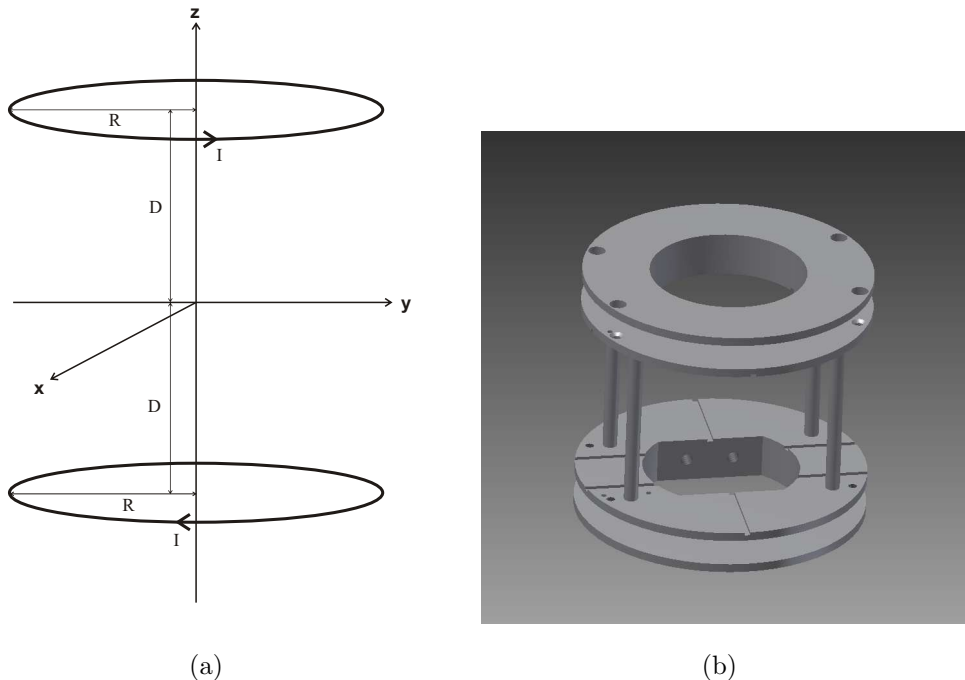


Figure 4.1.: a) Sketch of a pair of coils in anti-Helmholtz configuration. b) CAD drawing of the mechanical frame for the quadrupole coils. Courtesy of Julian Hofmann.

coils as depicted in figure 5.6(b). The criterion for designing this coil-pair is the magnetic field gradient it generates at the trap region, which will determine the trapped atom density at that region [17]. As can be derived from elementary magnetostatics, the magnetic field gradient in the axial direction at the center of an anti-Helmholtz coil is given by:

$$\frac{\partial B_z}{\partial z} \Big|_{z=0, \rho=0} = 3\mu_0 N I \frac{DR^2}{(D^2 + R^2)^{5/2}}, \quad (4.1)$$

where D and R are the half of the distance between the two coils and the radius of them respectively, N is the number of windings and I the current passing through the coils (see fig. 5.6(a)). A more sophisticated mathematical treatment is needed to obtain the field components at points off the z -axis (see A.2.1). It can be shown that in the ideal anti-Helmholtz configuration, $2D=R$, the field gradient will reach its maximum. However, there is a trade off between the size and the windings of the coils. In order to meet the experimental requirements, the quadrupole coils are expected to generate a field gradient of 7 G/cm with 1 A current supply in the axial

direction [17]. Additionally, the distance between the coils, $2D$ in this context, is restricted by the glass cell which has a height of 42 mm. Therefore, as one can see from eq. 4.1, the only parameters left are the radius of the coils and the number of windings.

Our calculation indicates that for constructing an ideal anti-Helmholtz coil-pair under the restrictions mentioned above, more windings for the coils will be needed, which will lead to heating problems.

At the end, the dimensions of the coils are made such that instead of having an ideal anti-Helmholtz configuration, they are all kept as small as possible so that a reasonable amount of windings will be sufficient to generate the desired field gradient. Inserting the values $D=35$ mm, $R=40$ mm, $I=1$ A and $\frac{\partial B_z}{\partial z}=7$ G/cm (or $\frac{\partial B_\rho}{\partial \rho}=3.5$ G/cm), we obtain $N=140$.

4.1.2. Compensation coils

In order to offset external magnetic fields, such as the Earth's magnetic field, the field from power supply lines and so on, a compensation system consisting of three pairs of coils in Helmholtz configuration is built. These coils are sustained by a cubic mechanical frame and oriented along the three spatial axes, each of them is designed to be able to provide 500 mG uniform magnetic field at the center of the trap. Instead of the copper wire which is used for the quadrupole coils, 16-way ribbon cable (also known as multi-wire planar cable) is used for the compensation coils. These conducting wires are much thinner than usual copper wires hence having lower capability of carrying current. The number of windings is determined such that the above mentioned offset fields can be generated with 50 mA current supply. This requires 13 turns of the ribbon cable for the square frames and 16 for the rectangular ones, see appendix A.2.2 for the calculation. The current passing through each pair of the coils will be supplied independently; a three output DC current source is built for such need.

4.2. Preparation of the MOT beams

Besides cooling atoms, each pair of the MOT beams have to be circularly polarized with orthogonal polarization in order to confine atoms in the central region (see section 3.2). Polarization-maintaining fibers (PM fibers) are used to guide laser beams to the MOT. By launching linearly polarized beams onto one of the two polarization preserving axes combining with a quarter-wave plate at the output, the desired circularly polarized beams can be obtained. In the following, preparation of the six MOT beams and characterization of the relevant components are described.

4.2.1. Cooling and repump laser systems

As mentioned in chapter 2 two laser frequencies are needed for the cooling process. They are the cooling and repump beams which address the $F = 2$ to $F' = 3$ and the $F = 1$ to $F' = 2$ transitions respectively. Both of them are derived from commercial laser diodes and optically stabilized by means of feedback from diffraction gratings [34]. These laser diodes are driven by a commercial laser diode controller¹ which also provides an adjustable PID temperature control loop. The frequency of the laser diode is stabilized by Doppler-free saturation spectroscopy technique. Using such technique spectral linewidth of 0.6 MHz is achievable [17, 23], which is an order of magnitude smaller than the natural linewidth ($2\pi \cdot 6.067\text{MHz}$ [35]) of the D_2 line.

Acousto-optic modulators

Acousto-optic modulators (AOM) are used through out the experiment. An incident laser beam onto an AOM can be diffracted from a moving acoustic wavefront. The power of the output beam depends on the power of the propagating acoustic wave which is dependent on the RF signal sent into the modulator. Customized circuits are built to generate and control the level of the RF modulation signal and provides a mean to control the power of a laser beam.

For the purpose of cooling, AOMs are used to switch on and off and to control the optical power of the cooling and repump beams.

4.2.2. Optics for six arms splitting

To achieve the best cooling effect the intensity between the two counter-propagating cooling beams should be balanced. In both of the old traps, a retro-reflecting scheme is used [17] - three incident beams are back-reflected into themselves. It is a convenient way to generate counter-propagating beam-pair, however, since the cooling beams have to pass through the glass cell several times, the back-reflected beams will inevitably loose a little amount of power. In this new setup, instead of the retro-reflecting technique, the cooling and repump beams are split up into six beams before being overlapped in the trap. This section will describe how this is done in our lab, as well as the characterization of components such as the polarization-maintaining fiber and the feedback circuit which are critical to produce well-polarized and power stable cooling beams.

Polarization-maintaining fiber

All lasers are set up on a separate optical table and connected by optical fibers to the one where the trap is situated. Polarization-maintaining fibers are used to avoid

¹Thorlabs ITC 102

drifts of polarization of the laser beams. Two commercially available PM fibers²³ (both suited for the $\lambda=780\text{nm}$ wavelength) have been tested in order to find out which one performs better under our experimental condition.

Optical fibers always exhibit certain degree of birefringence, which leads the polarization of light propagating in the fiber gradually changes in an uncontrolled way, and are also sensitive to mechanical stress and temperature. A PM fiber, which is not a fiber without birefringence, can fix the problem by introducing a strong built-in birefringence. Provided that the polarization of light launched into the fiber is aligned with one of the two birefringent axes, the polarization state will be preserved. The figure of merit of these fibers is the low cross-coupling of optical power between different polarization modes, when the polarization of the incoming light is oriented correctly. We characterized this by measuring a polarization extinction ratio - the fraction of incorrectly polarized light in terms of optical power - in a simple setup depicted in fig. 4.2. A well defined linearly polarized beam whose polarization direction is aligned with one of the polarization preserving axes is coupled into the fiber⁴. The extinction ratio is then taken as P_B/P_A , the power measured at position B divided by that measured at A, when P_B is minimized. It turns out that for both of these fibers the measured extinction ratio can reach 1/1000. Nevertheless, in order to test their sensitivity to mechanical stress and temperature, we perform the same measure when they are heated and twisted. The measurement shows that the one from Newport has less cross-coupling - the extinction ratio of it varied between 1/1000 and 1/600 while the one from Schäfter+Kirchhoff varied from 1/1000 to 1/500. However, both of them are sufficient for the purpose of guiding cooling beams.

Splitting of laser beams

After the cooling and repump beams are guided to the optical table for the trap, they are coupled into one on a polarizing beam⁵ splitter and then split up into six branches for the optical molasses as shown in fig. 4.3. At the end all six beams are coupled into PM fibers and guided to the MOT (see fig. A.3). The remaining beam is split up into the cooling and repump beams again by a polarizing beam splitter and monitored separately by photodiodes. With the signals from those diodes we stabilize the power of each of the beams by a feedback loop.

The actual procedure for aligning this arrangement can be divided into two steps.

²Newport F-PM630, with nominal mode field diameter $4.5\pm 0.5 \mu\text{m}$

³Schäfter+Kirchhoff PMC780

⁴To ensure the polarization mode matching, the half-wave plate and the polarizer 2 shown in fig. 4.2 are rotated such that the light power measured at position B is minimized.

⁵This is done by rotating the half-wave plates in front of the fiber couplers such that the polarization of cooling and repump beams are oriented horizontally and vertically, respectively (see fig. 4.3).

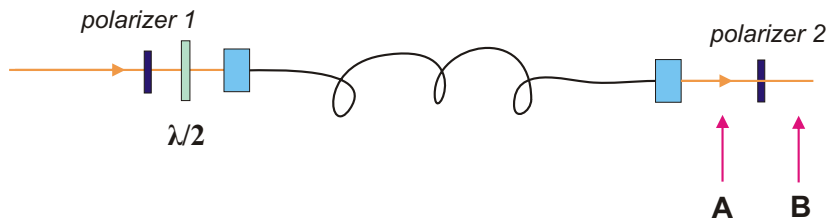


Figure 4.2.: To characterize a p-m fiber, a linearly polarized light whose polarization direction matches one of the polarization preserving axes of the fiber is coupled into the fiber. This is done by rotating the half-wave plate ($\lambda/2$) shown in the graph. Polarizer 1 and 2 are used to purify the polarization of the incoming beam and to analysis the outgoing beam, respectively.

First, the cooling beam is used to align all the components and optimize the coupling efficiency into the six fibers. Afterward, the second beam is overlapped with the first one at the PBS. The criterion for optimizing the overlap is the coupling efficiency of the second beam into the six fibers. At the end, we managed to couple around 80% of cooling light and 65% repump light into all six fibers. Since the 50:50 beam splitters⁶ we used have 55:45 splitting ratio for 780 nm (both p- and s-polarization) light, six beams with equal intensity are hard to achieve. However, what is important for the optical molasses is the same intensity of each pair of opposing propagating beams. Therefore, we group these six beams into three pairs and adopt a method using a PBS and a half-wave plate to actively equalize the amount of power coupled into each pair of fibers. The cooling and repump beams are linearly polarized and orthogonal to each other, their polarization direction can be rotated by using a half-wave plate. Since a PBS transmits horizontally polarized light and reflects vertically polarized one, the laser power split up by the PBS can thus be controlled by the half-wave plate.

Power stabilization

The three laser beams involved in this thesis, the cooling, repump and dipole trap beams, are power regulated via a same kind of feedback loop. The optical power of the beams are controlled by AOMs. In the experiment, a custom stabilization circuit compares the actual light voltages obtained by a photodiode in the setup to a reference voltage; a control signal is then sent to change the RF signal feeding in the AOM and results in changing the laser power towards the reference level.

A time constant of the stabilization circuit has to be set properly. The purpose of this circuit is to stabilize the laser power for long period of time against unwanted fluctuations, such as decreasing coupling efficiency of fibers and AOMs. Typically,

⁶Thorlabs BS011

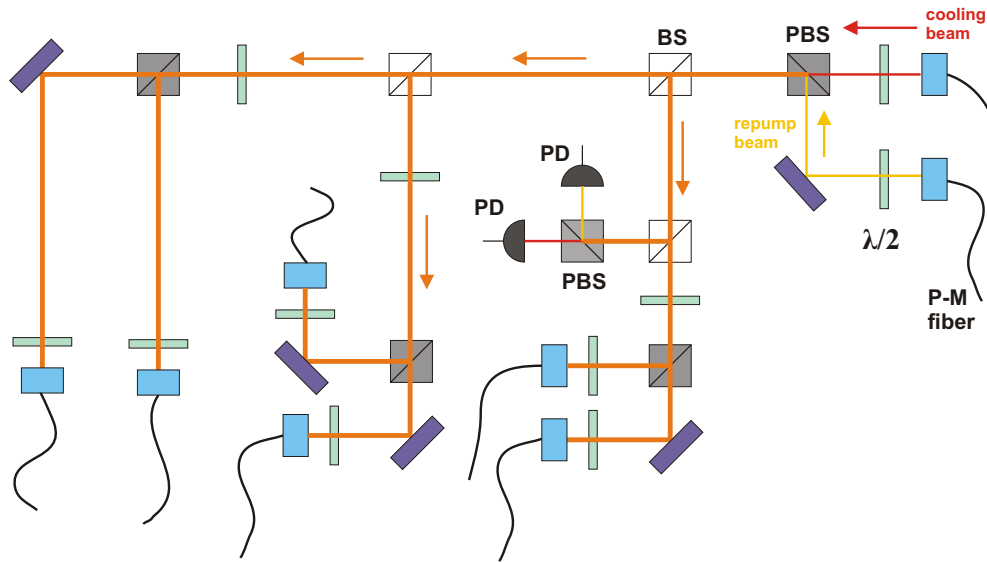


Figure 4.3.: Sketch of the optics for the six arms splitting. The cooling and repump beams, with orthogonal polarization, are coupled into one beam on a polarizing beam splitter (**PBS**) first and then split up step by step by 50:50 beam splitters (**BS**) and **PBSs** into six branches. Two photodiodes (**PD**) are implemented to monitor the power of the cooling and repump beams.

the time scale is several seconds to hours. However, during the optical pumping and excitation cycles of single atoms as mentioned in section 2.3, the cooling beam will be switched on and off under a $2\mu\text{s}/1\mu\text{s}$ cycle [23]. The stabilization circuit is not design to catch up such fast switching, yet, if the time constant of it is set too small, this process will cause the circuit to oscillate. With this consideration in mind, the response time of this circuit is slow enough, such that the fast switching is ignored. Figure 4.4 shows the testing result of the stabilization circuit under the condition simulating the above mentioned process. A test with long time scale shows (several seconds) that the stability of this circuit is about 7%.

4.3. Summary

This chapter presents the construction of the magneto-optical trap. Magnetic coils are built in such a way to provide sufficient field gradient at the center (quadrupole coils, $7\text{ G/cm}\cdot\text{I}$ in axial direction) and uniform filed in the three spatial axes direction (compensation coils, 10 mG/mA) in order to fit the experimental requirements. The MOT beams consisting of cooling and repump beams are prepared. Each of

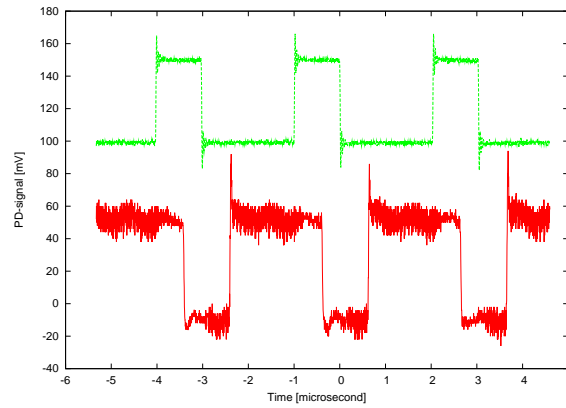


Figure 4.4.: Testing results of the power regulation circuit. The laser power is monitored by a photodiode while the laser is switched on and off by the control signal (upper signal on the graph).

them are split into six branches, and then guided to the MOT by PM fibers. An additional branch is used for monitoring and actively stabilizing the laser power by a feedback loop. The regulation circuits are also built and characterized so that they can regulate the laser power properly for long time scale without causing problems during fast switching.

5. Single atom trap

In our experiment, the single atom trap for ^{87}Rb is generated by a strongly focused laser beam using a commercially available microscope objective. Besides the dipole trap laser, the ionization laser and the collection optics for detecting fluorescence light from the trap region are the other two key elements. Since single atoms are trapped at the focus point of the dipole trap beam, the focus of the ionization beam and the effective region of collection optics should be overlapped with the focus of the trap beam in order to achieve the best performance - high ionization rate and collection efficiency of emitted photons. An optical arrangement, so-called confocal microscope, is used to achieve such goal. An aligning laser beam is used to simulate the imaging properties of collection optics, and the focus of this beam is considered as the effective region for collecting photons. In this chapter the experimental implementation of the dipole trap will be treated in detail. The preparation of the dipole trap beam is presented first. In the second part of this chapter, construction of the confocal microscope and the procedure of overlapping the foci of the beams are described.

Additionally, obtaining more laser power for ionization using laser diodes is an ongoing investigation to improve the atomic state detection scheme. Some of the potential candidates are laser diodes with shorter emission wavelength compared to the previously used 473 nm continuous wave (CW) laser. This is also taken into account when characterizing the components relevant to the blue laser.

5.1. Dipole trap laser

The dipole trap laser used in our experiment is also built from a laser diode¹ with a wavelength of 852 nm. Since the laser frequency for this laser is not so critical as for the cooling and repump lasers, the sophisticated frequency locking technique described in sec. 4.2 is not needed here. However, the same mechanical parts for holding the diode and the collimation lens etc., is used. This laser diode has a beam divergence of 30° (θ_\perp) and 9° (θ_\parallel) in the direction perpendicular and parallel to the polarization direction, respectively. A collimation lens² with NA=0.55 and f=4.5 is used to collect and collimate the light coming out of it. The laser diode is oriented

¹JDSU 5420 series

²Thorlabs C230TM-B

such that the θ_{\perp} direction is parallel to the breadboard. In order to get a symmetric beam profile a prism pair is used to compress the laser beam in the θ_{\perp} direction. A collimated beam with diameter around $900 \mu\text{m}$ is thus obtained.

The diode has a threshold current of 35 mA and maximum output power of 150 mW with operating current of 210 mA. A similar laser diode controller³ as the one for cooling beam is utilized to provide the current supply and stabilize the temperature through a thermistor embedded in the same aluminum plate where the diode is situated. To protect the laser diode from any back reflections an optical isolator⁴ with an isolation of 34-40 dB is installed after the prism pair along the optical path of the laser beam.

5.1.1. Preparation of the trap beam

The dipole trap laser will be coupled into a polarization-maintaining fiber and guided to the confocal microscope to generate the strongly focused single atom dipole trap. In between, an AOM is set up to control the laser power. A small fraction of the laser power derived from the main beam by using a glass plate is sent into a cavity to monitor the laser mode. The cavity is arranged in a confocal configuration to monitor whether the laser operates in a single longitudinal mode, see fig. 5.1. With a length of 10 cm, the free spectral range of the cavity is 1.5 GHz. The cavity finesse can be approximated by

$$F \approx \frac{\pi\sqrt{R}}{1-R},$$

where R is the reflectivity of the mirrors. Using mirrors with 96% reflectivity gives the maximum value for cavity finesse of 77. The actual finesse, which is around 60, can be obtained by inspecting the cavity signal (fig. 5.1).

An AOM⁵ is set up to control the intensity of the trap beam. By coupling light into the first diffraction order, the AOM can be used to switch and vary the power of the trap laser coupled into the fiber. A lens with $f=125$ mm is used to focus the beam onto the AOM since the switching time of an AOM is related to the beam size within the crystal. Under optimum conditions, the modulator has a rise time (10 to 90 percent) [36]:

$$T_r = \frac{0.66d}{V}, \tag{5.1}$$

where d is the optical beam diameter and V the acoustic wave velocity in the crystal (TeO_2 for the model we used). Using the propagation equation of Gaussian beam

³Thorlabs ITC 110

⁴Thorlabs IO-3D-850-VLP

⁵Crystal Technology, Model 3200-121

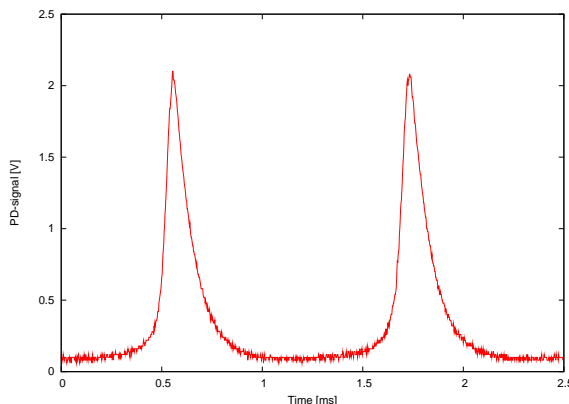


Figure 5.1.: Cavity signal of the dipole trap laser.

(3.16), the beam diameter in the crystal is estimated to be around $160 \mu\text{m}$ (the TeO_2 crystal is around 115 mm from the focus lens). With this value and the acoustic wave velocity of TeO_2 4.26 km/sec , the rise time is around 25 ns according to eq. (5.1). The actual test shows that the rise time for the optical power to increase from 10 to 90% is around 30 ns in our experimental condition. The coupling efficiency of the power into the first diffraction order of the AOM is optimized to 75 %.

A PM fiber is used to guide the laser to the single atom trap setup. It has a core diameter of 5 microm and a built-in silicon detector used to monitor the laser power transmitted through the fiber. Using the method described in sec. 4.2.2, the extinction ratio of this fiber is measured to be $1/300$.

5.2. Confocal microscope

The confocal microscope in our experiment consists of three components: the dipole trap laser, the ionization laser and the collection optics for collecting light emitted from ^{87}Rb atoms. The detailed procedure of how the microscope is constructed will be presented in this section. The collection optics is supposed to collect single photons emitted in the entanglement generation process as well as the fluorescence light from the atoms when cooling beams are shined on them. Both of them have the wavelength of $\lambda=780 \text{ nm}$. The ionization laser used for atomic state detection in one of our previous traps was a blue laser with wavelength 473 nm . All these three beams are strongly focused by an objective⁶ with a numerical aperture of 0.5 and a working distance of 13.89 mm . The advantages of having the smallest

⁶Mitutoyo G Plan Apo 50

possible foci for the three optical beams are the following:

- *Collection optics:* Due to the limited numerical aperture, only a relatively small amount of photons emitted from the atoms can be collected. However, by increasing the focusing of the detection optics, this number can be increased. This is particularly important for detecting the single photons emitted in the Λ -decay process.
- *Dipole trap laser:* A strongly focused dipole trap beam has the advantage that up to a certain loading rate no more than one atom is loaded into the trap due to the blockade mechanism (see section 2.2).
- *Ionization laser:* A small focus for the ionization laser is also favorable, since an atom can be ionized faster with higher light intensity (see section 2.4).

The laser power for ionization is critical for fast analysis of the atomic state. A 445 nm blue laser diode has been set up to replace the 473 nm CW laser. By driving this diode with short electronic pulses above specified value, the power of the ionization pulses can be pushed to 100 mW [37]. Because of this rather promising method to achieve high ionization laser power, a 450 nm blue laser diode is set up, instead of using the 473 nm one, for aligning the microscope.

Besides the microscope objective, another key ingredient of the microscope are the dichroic mirrors used to separate light from the three different wavelength. Two dichroic mirrors are used for the microscope - one optimized for reflecting light with 780 nm wavelength, transmitting the 850 nm and 473 nm ones (*HR780*); the other optimized for reflecting 850 nm and transmitting 473 nm ones (*HR850*). Since, in atom-photon entanglement, the information of the photonic qubit is encoded in the polarization state, the reflectivity difference between different polarization states should be as small as possible. We expect that the reflectivity of the *HR780* mirror for different polarizations changes under different angle of incidence [38]. As a result, this dichroic mirror has to be characterized first and the result will be described in the first subsection. For testing these dichroic mirrors and the subsequent alignment of the collection optics, the cooling laser which has the wavelength of 780 nm is used.

The foci of the dipole trap, ionization beams and the collection optics must be superimposed at the center point of the MOT. If not, the collection efficiency of the light from trapped single atoms and the ionization probability of the atoms will decrease. Therefore, proper alignment of the optical paths of these optical beams is important and will be the main subject of the last two subsections.

5.2.1. Dichroic mirrors

One important measure of the *HR780* mirror for our purpose, as mentioned above, is the indistinguishability of the s- and p-polarized light with 780 nm wavelength. The orientation of this mirror, consequently the incident angle of the 780 nm beam, is critical for detecting the spontaneously emitted photons from the entanglement process. Since the *HR780* mirror is the component on which all three beams will be overlapped (see fig. 5.4), one has to take into account the effect of its orientation on the other beams. Ordinarily, the power of the dipole trap laser is always sufficient for the experiment, this leaves only the ionization laser to be tested along with the 780 nm laser.

A simple test is carried out in the way shown in fig. 5.2, where the transmission of the *HR780* mirror is measured using laser beams with 780 nm and 450 nm wavelength under different angle of incidence. The beam paths are arranged in the same way as in the actual setting of the microscope. The incident angles of the two beams are the same as indicated in the sketch. The results is summarized in table 5.1.

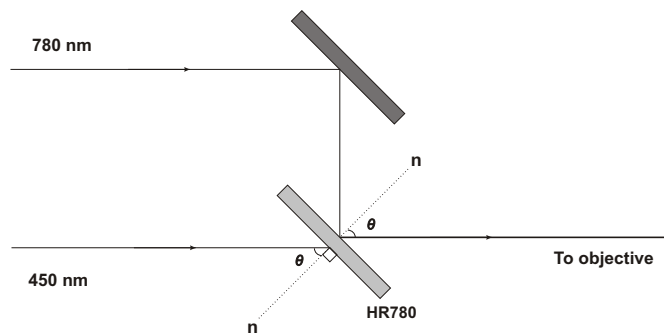


Figure 5.2.: The angular relation of the 780 nm and the 450 nm beams for testing the *HR780* mirror.

θ	Transmission (%)	
	780 nm (p-state)	450 nm
35°	0.087	85
40°	0.13	93.4
45°	0.35	96
50°	-	79

Table 5.1.: Testing results of the *HR 780* dichroic mirror.

The results of the 780 nm s-polarized light is not shown because it is almost always 100% reflected under different incident angles (with less than 0,01% of light

transmitted). The transmission of the 450 nm beam is recorded with the p-polarized light which has the maximum power transmitted through the mirror. At the end, we decide to use the angle $\theta = 45^\circ$ - which provides already good indistinguishability between the two polarized state and has the highest transmission rate for the blue laser. Research in our group shows that some laser diodes with even shorter wavelength might be able to provide more ionization power. Due to this future interest, we measured the transmission spectrum of the *HR780* mirror for shorter wavelength using a spectrometer, see fig. 5.3.

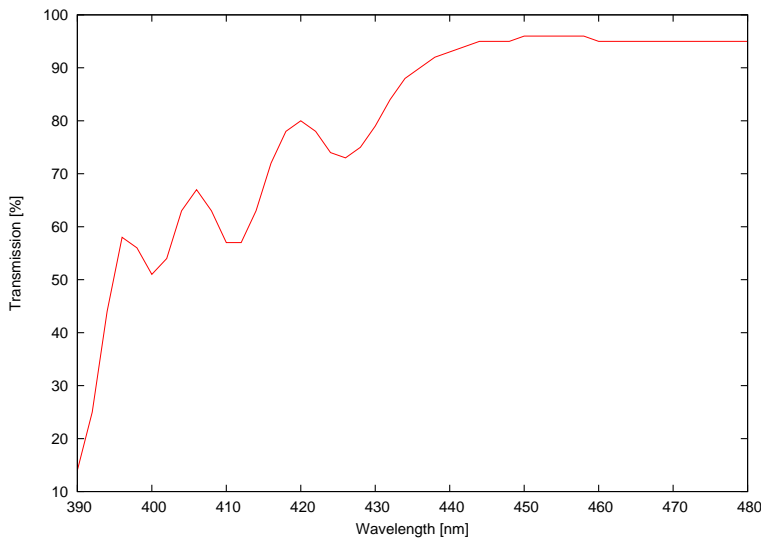


Figure 5.3.: Transmission spectrum of the *HR780* dichroic mirror with a 45° angle of incidence.

5.2.2. Optical alignment

A schematic drawing of the microscope setup is shown in figure 5.4. All the light beams are guided to or from the microscope by single mode fibers^{7 8} (polarization-maintaining fiber for the trap beam, see 5.1.1). The trap beam and the ionization beam are overlapped on the *HR850* mirror first, they are then overlapped with the collection optics on the *HR780* mirror. All these three beams are focused by the objective.

⁷Thorlabs 780HP, for collection optics

⁸Thorlabs S405-HP, for blue laser

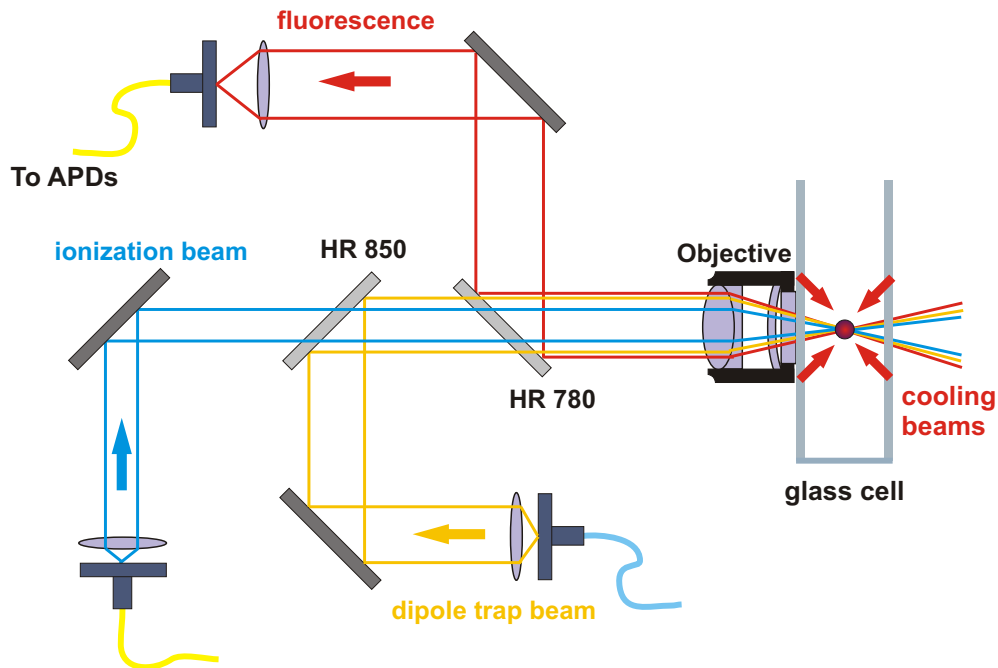


Figure 5.4.: Schematic drawing of the microscope setup. The optical paths of the dipole trap (856 nm), ionization beams (450 nm) and the collection optics (780 nm) are altogether superimposed onto the optical axis of the microscope objective. By moving the breadboard on which the setup is constructed, the focus of the microscope can be placed at the center of the MOT. Fluorescence photons from single atoms will be detected by avalanche photodiodes (APDs).

The entire structure is built on a separate breadboard (see fig. A.3). This design allows us to assemble the microscope and adjust it independently, and incorporate it with the vacuum apparatus and MOT at the final stage. At the beginning of designing the new trap, the height of the laser beams with respect to the breadboard was decided; the mechanical frames for the MOT were designed accordingly. While constructing the microscope, every optical beam path is adjusted to this standard beam height. At the end, by shifting the entire breadboard with respect to the glass cell in the horizontal plane, the focus of the microscope can be coincided with the center point of the MOT. The optical alignment of the confocal microscope can in principle be divided into two parts: aligning the collection optics with respect to the objective and overlapping the beam path of the trap and ionization lasers with that of the collection optics.

Adjusting the collection optics

The cooling beam with wavelength 780 nm is used as the aligning laser for the collection optics and is sent through the fiber in the direction opposing the fluorescent direction from single atoms. A collimated beam with radius of $730 \mu\text{m}$ is obtained by using an out-coupling lens of focal length $f = 11\text{mm}$. The beam waist w_0 of the aligning laser at the focus of the objective is simulated as the cross-sectional radius of the effective region of collection optics. The procedure to overlap the beam path of the collection optics onto the optical axis of the objective is as follows:

- The first thing to do is to mount the objective onto the breadboard. It is screwed onto an L-shaped aluminum plate which is mounted on a translational stage so that the height of the objective can be adjusted to match the standard beam height. Typically, the distance between the objective and the glass cell is kept around 1 to 2 mm, and has to be taken into account when positioning the objective.
- The objective should be mounted so that its optical axis is parallel to the surface of the breadboard. This can be done by adjusting the aluminum plate, where the objective will be mounted on, so that the surface normal of the plate is parallel to the breadboard. The parallelism of the optical axis of the objective and the surface normal of the plate is assured by the mechanical design of this plate.
- The beam path of the aligning laser can be rather accurately adjusted to overlap with the optical axis of the objective with the help of two points. The first one is the aperture of an iris screwed on the same socket where the objective is mounted on; the second one is the focus point of the objective. To make use of the focus, the objective is first removed from the socket. Then, a mirror is set up on a translational stage that moves in the direction of the laser propagating direction at the vicinity of the focus position. With the help of a second iris installed along the beam path of the aligning laser, this mirror can be adjusted to reflect the aligning laser back along the same path. The objective is then screwed back into the socket, and the mirror on the translational stage is moved toward the focus of the objective. By iteratively adjusting the beam spot on the two aperture, the reflected beam from the mirror can overlap with the incoming beam. This guarantees that the aligning laser passes through the optical axis of the objective.

Adjusting the trapping and ionization beams

After the collection optics is aligned with respect to the optical axis of the objective, the dipole trap and the ionization beams also need to be overlapped onto the same axis. The dipole trap laser and the ionization laser are both collimated by lens of

focal length $f = 6.2$ mm but with different anti-reflection coating. The obtained collimated beams have $w_0 = 730 \mu\text{m}$ and $w_0 = 560 \mu\text{m}$ for trap and ionization beams, respectively. The trapping and the ionization beams are superimposed with the aligning laser by coinciding the beam spots at two positions 4 meter apart.

5.2.3. Overlapping the foci of the beams

Due to chromatic aberration of the objective, the z-positions of the foci of the three beams may differ. To correct this deviation, the z-position of the foci must be determined and then adjusted. The determination of the focus position (z-position) of each beam as shown in fig. 5.5 is a two step process. While a razor blade, which

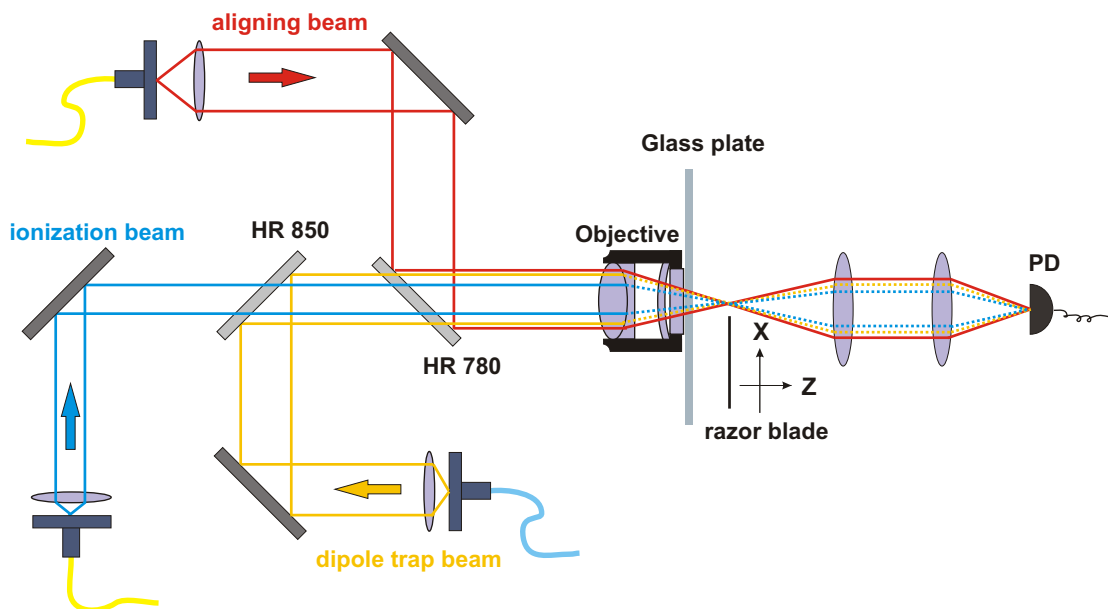


Figure 5.5.: Schematic illustration of the procedure to overlap the foci of laser beams. After passing through the objective the laser beams are collimated and focused on a photodiode. A glass plate, which is made from the same material with the same thickness as the glass cell is inserted in front of the objective.

is mounted on a set of stepper motors and oriented perpendicularly to the propagation direction of the beams, is moved transversely into the beam (x-direction in the diagram); a photodiode records the remaining light power. By doing so, the dependency of the intensity of a laser beam on the x-position of the razor blade at any z-position can be measured. For a Gaussian beam, the integrated power as a

5. Single atom trap

function of x-position of the razor blade is given by [38]:

$$P(x) = P_0 + \frac{2P}{\pi w^2(z)} \int_{-\infty}^x dx \int_{-\infty}^{\infty} dy e^{-\frac{2(x^2+y^2)}{w^2(z)}} = P_0 + P_1 \operatorname{erf} \left(\frac{\sqrt{2}(x - x_0)}{w(z)} \right), \quad (5.2)$$

where the parameters P_0 and P_1 describe the background light power and the power of the laser respectively. Applying a least squares fit to this function via the measured data, the radius of the beam $w(z)$ and the x-position of the peak intensity x_0 can be determined. By repeating this procedure at different longitudinal positions, one obtains a set of beam radii versus z-positions. With this set of data, the z-position of the foci z_0 can be determined precisely by fitting them to the function

$$w(z) = w_0 \sqrt{1 + \frac{M^4(z - z_0)^2}{z_R^2}}, \quad (5.3)$$

where z_R is the Rayleigh length and M^2 is the beam propagation factor [39] used to characterize a real laser beam containing higher TEM modes. By slightly shifting the collimation lens in fiber collimators, the divergence of the laser beams can be changed resulting in the position shifting of their foci. Repeating the process of determining z_0 and tuning collimation lenses, the foci of the dipole trap and the ionization beams can be overlapped with that of the collection optics.

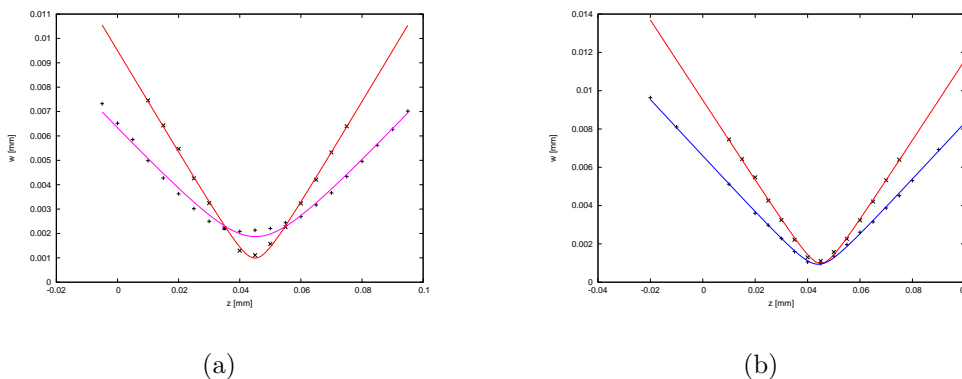


Figure 5.6.: Beam radius $w(z)$ measured as a function of z-position for the three wavelengths: 780 nm (red), 856 nm (pink), 450 nm (blue). The solid lines are the least-square fit of the measured values according to equation 5.3. The data points were taken after the three foci were overlapped.

Wavelength	z_0 (μm)	x_0 (μm)	w_0 (μm)
780 nm	0 (def.)	0 (def.)	1.00 ± 0.06
856 nm	$+0.4 \pm 0.4$	$+0.2 \pm 0.05$	1.83 ± 0.04
450 nm	-0.5 ± 0.1	$+0.9 \pm 0.02$	1.14 ± 0.04

Table 5.2.: Data of the foci positions of aligning, dipole trap and ionization beams. Focus position of the aligning beam is defined as the zero point.

5.3. Summary and discussion

In this chapter the construction and characterization of the single atom trap are presented. A confocal microscope is set up to precisely overlap the foci of the three relevant optical beams. The linearly polarized dipole trap beam is prepared and then coupled into a PM fiber guiding to the trap setup. Cavity used to monitor the laser mode and AOM for controlling the laser power were set up. The coupling efficiency of the AOM and the optical fiber were all optimized in order to obtain maximal laser power at the trap region.

The total transmission loss between the output of the fiber and the trap region is around 50%. Taking into account the coupling efficiency of the AOM and fiber together with losses from other optical components, laser power of 15 mW at the trap region is achievable. The trap depth can be estimated by using equation 3.18 with available power $P=15$ mW at the trap region, $w_0=1.83$ μm and $\lambda=856$ nm:

$$U_0 = 1.6 \text{ mK.}$$

As mentioned already, a 445 nm blue diode laser with maximum available power of 100 mW is set up in our group. The power loss tested with the 450 nm beam from the fiber output on the microscope to the trap region is about 40%. Thus, the maximum intensity of ionization laser at the trap region achievable with the 445 nm laser can be estimated from $2P/(\pi w_0^2)$ with w_0 being the beam radius:

$$I_{ion} = 29.4 \times 10^8 \text{ mW/cm}^2.$$

Compared to the demonstration in [19] with 32.8 mW ionization power, an even faster ionization rate can be expected.

6. Summary and outlook

This thesis describes preliminary steps made toward the construction of a single atom trap. This new single atom trap is designed to incorporate a fast atomic state analysis scheme which is a crucial part for performing a loophole-free Bell test.

To successfully trap single atoms, a magneto-optical trap and an optical dipole trap have to work jointly with the former working as a cold atoms reservoir for loading a single atom into the dipole trap. Magnetic coils and the six cooling beams for the MOT are prepared. The quadrupole coils are able to provide 7 G/cm and 3.5 G/cm magnetic field gradient with 1 A current supply in the axial and radial direction, respectively; the compensation coils can provide 500 mG with 50 mA along each of the three spatial axes. The six MOT beams are prepared; together with an optical arrangement of a combination of PBS and half-wave plate we can actively balance the intensity between each two of the counter-propagating beams.

The dipole trap beam is also prepared. By optimizing the coupling efficiency of the AOM and fiber, 15 mW laser power is available at the trap region yielding a trap depth of $U_0=1.6$ mK. In order to keep the depth of the potential constant, the intensity of the trapping beam is continuously monitored and stabilized by a feedback loop. A confocal microscope is built. The microscope objective strongly focuses the three relevant optical beams to a few microns. By means of the method described in sec. 5.2, the foci of the dipole trap beam, ionization beam and the effective region of the collection optics can be overlapped.

Outlook

Besides implementation of the fast atomic state detection scheme, other efforts are made to improve the performance of the experimental setup. One inch post and specially selected mirror mounts are used for the entire construction. It is expected by using these components their mechanical vibration due to temperature fluctuation can be reduced, thereby the stability of optical beams can be improved.

Unlike the previous two traps, the cooling and repump beams are split into 6 beams instead of 3. Additionally, to improve the stability of the MOT, we decide to use cooling beams with larger diameter (compared to the two previous MOTs). This is done by using collimation lens with larger focal length ($f=18$ mm) for the output fiber collimator of MOT beams. The idea is that if a pair of opposing beams are not perfectly aligned, the percentage of misalignment is smaller with a larger beam, and the effect on the trapped atoms will be less significant [40]. To achieve these

improvement the laser power is more demanding. A high power semiconductor optical amplifier (Toptica BoosTA) is purchased to meet this need. With this amplifier the power of the cooling laser can be amplified to 1 W. However, an effect called stimulated Brillouin scattering will limit the amount of power that can be coupled into fibers. When a high power laser beam passes through a fiber it interacts with acoustical vibration modes in the glass, and causes a scattering mechanism that reflects much of the light back to the source. It is recommended by the fiber manufacturer to perform a preliminary test before launching the full power into the fibers in the setup.

To conclude, a magneto-optical trap and an single atom trap have been constructed. With critical requirements achieved - magnetic fields gradient for the MOT and intensity balance between cooling beams, laser power and waist diameter of the trap and ionization beams, it can be expected that once the the implementation of the glass cell (with CEMs inside) is finished, single ^{87}Rb atoms can be trapped in this new setup.

A. Appendix

A.1. Density matrix and optical Bloch equations

As an alternative to the wavefunction $|\Psi\rangle$, the density operator ρ , which is expressed as $\rho = |\Psi\rangle\langle\Psi|$, can also be used to describe the state of a system. It can be written in terms of a $n \times n$ density matrix with n the dimension of the Hilbert space. If a wavefunction $|\Psi\rangle$ is expanded by a complete basis set $\{\phi_n\}$ as

$$\Psi = \sum_{i=1}^n c_i \phi_i \quad (\text{A.1})$$

then the elements of the density matrix can be expressed as

$$\rho_{ij} = \langle\phi_i|\rho|\phi_j\rangle = \langle\phi_i|\Psi\rangle\langle\Psi|\phi_j\rangle = c_i c_j^*. \quad (\text{A.2})$$

For a two-level system the density matrix can be written down explicitly as

$$\rho = \begin{pmatrix} \rho_{ee} & \rho_{eg} \\ \rho_{ge} & \rho_{gg} \end{pmatrix} = \begin{pmatrix} c_e c_e^* & c_e c_g^* \\ c_g c_e^* & c_g c_g^* \end{pmatrix} \quad (\text{A.3})$$

and the time evolution of it depends on the Hamiltonian having the form

$$i\hbar \frac{d\rho}{dt} = [H, \rho]. \quad (\text{A.4})$$

Inserting eq. A.3 into eq. A.4 and taking into account the spontaneous emission, we obtain the optical Bloch equations:

$$\begin{aligned} \frac{d\rho_{gg}}{dt} &= \Gamma \rho_{ee} + \frac{i}{2} \Omega (\tilde{\rho}_{ge} - \tilde{\rho}_{eg}) \\ \frac{d\rho_{ee}}{dt} &= -\Gamma \rho_{ee} - \frac{i}{2} \Omega (\tilde{\rho}_{ge} - \tilde{\rho}_{eg}) \\ \frac{d\tilde{\rho}_{ge}}{dt} &= -\left(\frac{\Gamma}{2} + i\delta\right) \tilde{\rho}_{ge} + \frac{i}{2} \Omega (\rho_{gg} - \rho_{ee}) \\ \frac{d\tilde{\rho}_{eg}}{dt} &= -\left(\frac{\Gamma}{2} - i\delta\right) \tilde{\rho}_{eg} - \frac{i}{2} \Omega (\rho_{gg} - \rho_{ee}) \end{aligned} \quad (\text{A.5})$$

where Ω is the Rabi frequency and assumed to be real, which is true for transitions between bound states. Substituting the density matrix elements by the Bloch vector components:

$$\begin{aligned} u &= \tilde{\rho}_{ge} + \tilde{\rho}_{eg} \\ v &= -i(\tilde{\rho}_{ge} - \tilde{\rho}_{eg}) \\ w &= \rho_{gg} - \rho_{ee} \end{aligned} \tag{A.6}$$

where u and v represent the real and imaginary part of $\tilde{\rho}_{ge}$ respectively and w the population difference, the optical Bloch equations can be rewritten as

$$\begin{aligned} \dot{u} &= \delta v - \frac{\Gamma}{2}u \\ \dot{v} &= -\delta u + \Omega w - \frac{\Gamma}{2}v \\ \dot{w} &= -\Omega v - \Gamma(w - 1) \end{aligned} \tag{A.7}$$

The steady-state solution can be obtained by setting $\dot{u} = \dot{v} = \dot{w} = 0$:

$$\begin{pmatrix} u \\ v \\ w \end{pmatrix} = \frac{1}{\delta^2 + \Omega^2/2 + \Gamma^2/4} \begin{pmatrix} \Omega\delta \\ \Omega\Gamma/2 \\ \delta^2 + \Gamma^2/4 \end{pmatrix} \tag{A.8}$$

The steady-state population of the excited state can then be expressed as

$$\rho_{ee} = \frac{1 - w}{2} = \frac{\Omega^2/4}{\delta^2 + \Omega^2/2 + \Gamma^2/4} \tag{A.9}$$

A strong driving field ($\Omega \rightarrow \infty$) tends to equalize the populations, i.e. $w \rightarrow 0$.

A.2. Equations for magnetic coils design

In this section some detailed equations and calculations for magnetic coils design are provided. As mentioned in sec. 4.1 when dealing with the quadrupole coils, to obtain expressions for field components at off-axial points are not trivial. The expressions for the axial and radial components near the center point can be expanded into power series and are listed in the first subsection. The second subsection presents the detailed calculation for the compensation coils. In this section I represents the actual current supplied to the coils, N the number of windings.

A.2.1. Quadrupole coils

The magnetic field generated by a single coil can be calculated by integrating the vector potential \mathbf{A} over elements of each loop, and then apply $\nabla \times \mathbf{A} = \mathbf{B}$. For a single coil as shown in fig. A.1, the z and ρ components ($B_\phi = 0$) of the magnetic field at an arbitrary point can be expressed via complete elliptic integrals [41] and can be written down as a power series expansion near the origin.

The magnetic field components generated by two coils with radius R , placed $2D$ apart and with current I flowing in opposite direction can be written down as [42]:

$$B_z = \mu_0 N I 3 \frac{DR^2}{(D^2 + R^2)^{5/2}} z + \mu_0 N I \frac{15}{24} \frac{(4D^2 - 3R^2)R^2}{(D^2 + R^2)^{9/2}} (4z^3 - 6\rho^2 z) + \dots$$

$$B_\rho = -\mu_0 N I \frac{3}{2} \frac{DR^2}{(D^2 + R^2)^{5/2}} \rho + \mu_0 N I \frac{15}{16} \frac{(4D^2 - 3R^2)R^2}{(D^2 + R^2)^{9/2}} (\rho^3 - 4\rho z^2) + \dots$$

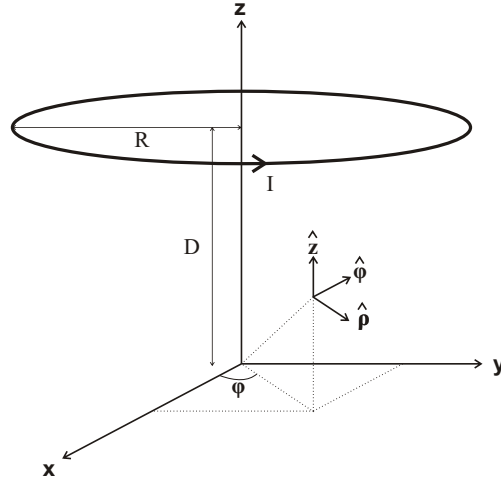


Figure A.1.: A single circular current loop centered at the z axis distance D above the origin represented in cylindrical coordinates.

The most notable feature from the above equations is that the gradient (consider only the first order term) in axial direction is two times larger than that in the radial direction (this can also be seen from $\nabla \cdot \mathbf{B} = 0$). In the ideal configuration where $2D=R$, the gradient reaches the maximum value for both directions and gives the magnitude

$$\frac{dB_z}{dz} = 2 \frac{dB_\rho}{d\rho} = \mu_0 N I \frac{48}{25\sqrt{5}R^2} \quad (\text{A.10})$$

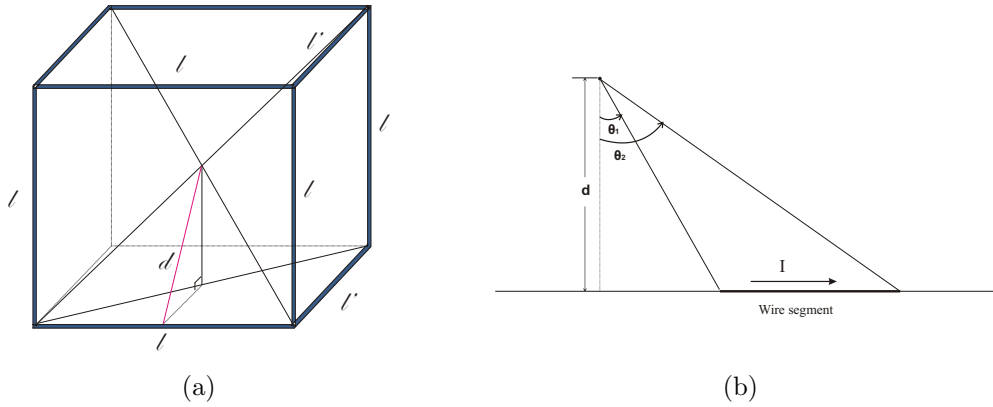


Figure A.2.: a) Schematic drawing of the frame of the compensation coils with dimensions labeled to be $l=22\text{cm}$ and $l'=19\text{cm}$. b) Illustration of the parameters used to represent the magnetic field created by a segment of wire.

A.2.2. Compensation coils

In our setup the compensation coils are supported by a cubic aluminum frame depicted in fig. A.2(a). The magnetic field produced by one pair of the coils at the center of this configuration is just the vector sum of the fields created by eight segmented current carrying wires. The magnetic field generated by a straight segment of wire carrying a steady current I at a distance d from the wire is given by [43]:

$$\mathbf{B} = \frac{\mu_0 I}{4\pi d} (\sin \theta_2 - \sin \theta_1) \quad (\text{A.11})$$

in terms of the initial and final angles θ_1 and θ_2 (see fig.A.2(b)). In our case, the center point is always on the perpendicular bisector line of each segment with distance d (two different cases as explained below) apart. Therefore eq. A.11, with $\theta_1 = -\theta_2$, becomes:

$$\mathbf{B} = \frac{\mu_0 I}{2\pi d} \frac{l}{\sqrt{l^2 + 4d^2}} \quad (\text{A.12})$$

There are two different kinds of geometry, namely square and rectangular frames, as shown in fig. A.2(a). Each pair of the Helmholtz coils will create a uniform magnetic field at the vicinity of the center and can be expressed as

$$\mathbf{B} = \frac{4\mu_0 I}{\pi} NG \quad (\text{A.13})$$

where G is a geometric factor which depends on the dimensions. For the square and rectangular frames, labeled 1 and 2 respectively, this factor can be written down

explicitly:

$$G_1 = \frac{2l^2}{(l^2 + l'^2)\sqrt{2l^2 + l'^2}} \quad (\text{A.14})$$

$$G_2 = \frac{ll'}{\sqrt{2l^2 + l'^2}} \left(\frac{1}{l^2 + l'^2} + \frac{1}{2l^2} \right) \quad (\text{A.15})$$

Inserting in the numbers $l=22\text{cm}$ and $l'=19\text{cm}$ and the desired maximum field $\mathbf{B}=500\text{ mG}$ with 50 mA current supply, we get $N_1=203$ for the square frames and $N_2=250$ for the rectangular ones.

A.3. Experimental setup

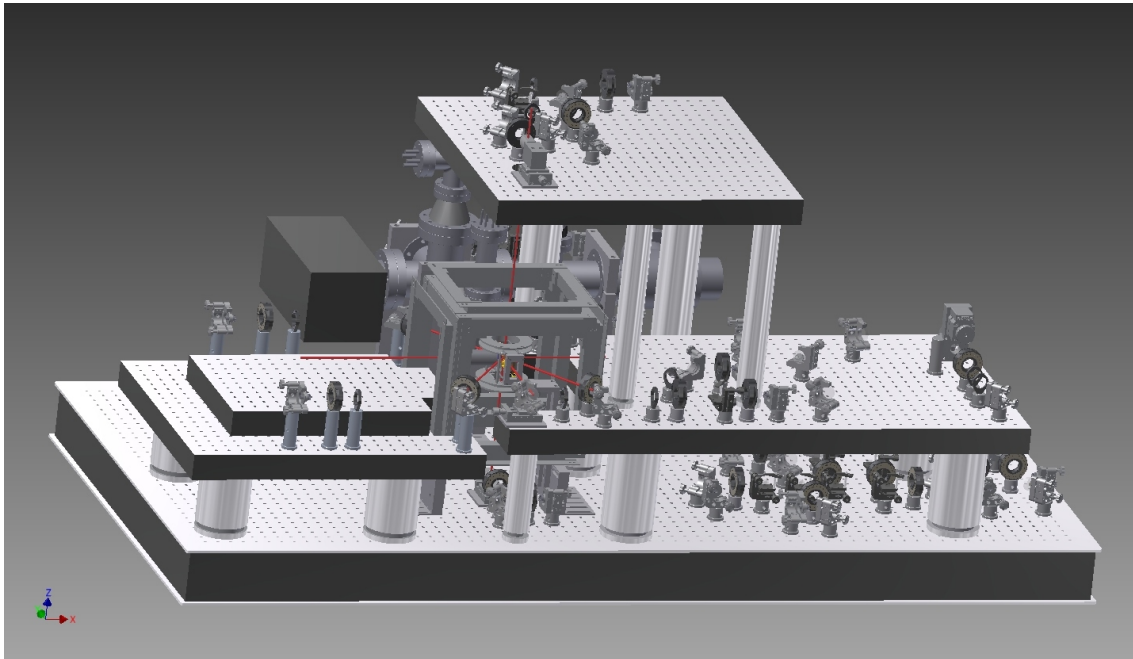


Figure A.3.: CAD drawing of the entire setup. The topmost breadboard on the left hand side of the MOT is the board for the confocal microscope. The lowest layer on the right hand side of the MOT is where the cooling and repump beams are overlapped and split up into six arms. Courtesy of Julian Hofmann.

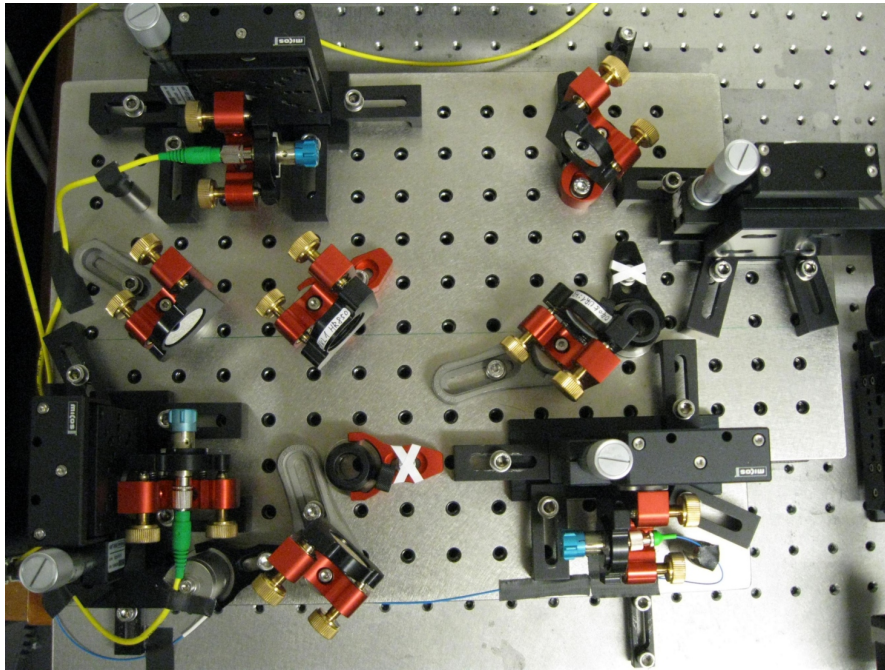


Figure A.4.: Photograph of the confocal microscope.

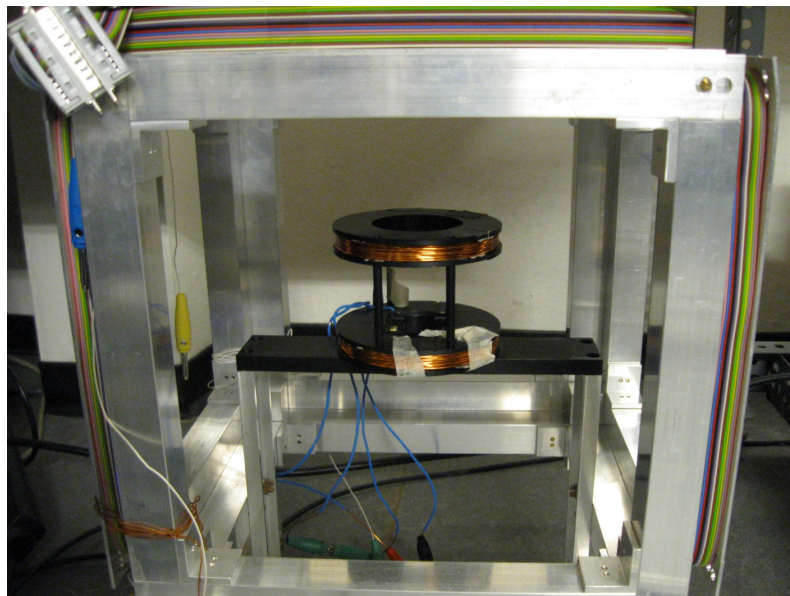


Figure A.5.: Photograph of the quadrupole and compensation coils.

Bibliography

- [1] A. Einstein; B. Podolsky; N. Rosen. Can quantum-mechanical description of physical reality be considered complete? *Phys. Rev.*, 47:777780, 1935.
- [2] D. Bohm. *Quantum Theory*. Prentice-Hall, Englewood Clis, New York, 1951.
- [3] J.S. Bell. On the Einstein-Podolsky-Rosen paradox. *Physics*, 1:195200, 1964.
- [4] S.J. Freedman; J.F. Clauser. Experimental test of local hidden-variable theories. *Phys. Rev. Lett.*, 28:938, 1972.
- [5] A. Aspect; P. Grangier; and Gérard Roger. Experimental tests of realistic local theories via Bell's theorem. *Phys. Rev. Lett.*, 47:460, 1981.
- [6] A. Aspect; P. Grangier; and Gérard Roger. Experimental realization of Einstein-Podolsky-Rosen-Bohm gedankenexperiment: A new violation of Bell's inequalities. *Phys. Rev. Lett.*, 49:9194, 1982.
- [7] G. Weihs; T. Jennewein; C. Simon; H. Weinfurter; A. Zeilinger. Violation of Bell's inequality under strict Einstein locality conditions. *Phys. Rev. Lett.*, 81:5039, 1998.
- [8] M.A. Rowe; D. Kielpinsky; V. Meyer; C.A. Sacket; W.M. Itano; C.Monroe; D.J. Wineland. Experimental violation of Bell's inequality with efficient detection. *Nature*, 409:791–794, 2001.
- [9] D.N. Matsukevich; P.Maunz; D.L. Moehring; S. Olmschenk; and C. Monroe. Bell inequality violation with two remote atomic qubits. *Phys. Rev. Lett.*, 100:150404, 2008.
- [10] M.A. Horne M. Zukowski, A. Zeilinger and A.K. Ekert. "Event-ready-detectors" Bell experiment via entanglement swapping. *Phys. Rev. Lett.*, 71:4287, 1993.
- [11] Christoph Simon and William T. M. Irvine. Robust long-distance entanglement and a loophole-free bell test with ions and photons. *Phys. Rev. Lett.*, 91:110405, 2003.

- [12] J. Volz; M. Weber; D. Schlenk; W. Rosenfeld; J. Vrana; K. Saucke; C. Kurtsiefer; H. Weinfurter. Observation of entanglement of a single photon with a trapped atom. *Phys. Rev. Lett.*, 96:030404, 2006.
- [13] F. Hocke. Long-distance atom-photon entanglement. Master's thesis, Ludwig-Maximilians-Universität München, 2007.
- [14] W. Rosenfeld; F. Hocke; F. Henkel; M. Krug; J. Volz; M. Weber; H. Weinfurter. Towards long-distance atom-photon entanglement. *Phys. Rev. Lett.*, 101:260403, 2008.
- [15] M. Weber. *Quantum optical experiments towards atom-photon entanglement*. PhD thesis, Ludwig-Maximilians-Universität München, 2005.
- [16] J. Volz. *Atom-photon entanglement*. PhD thesis, Ludwig-Maximilians-Universität München, 2006.
- [17] M. Krug. Atomic traps for efficient state detection of a single atom. Master's thesis, Ludwig-Maximilians-Universität München, 2007.
- [18] W. Rosenfeld; M. Weber; J. Volz; F. Henkel; M. Krug; A. Cabello; M. Zukowski; H. Weinfurter. Towards a loophole-free test of Bell's inequality with entangled pairs of neutral atoms. *Adv. Sci. Lett.*, 2:469, 2009.
- [19] F. Henkel; M. Krug; J. Hofmann; W. Rosenfeld; M. Weber; and H. Weinfurter. Highly efficient state-selective submicrosecond photoionization detection of single atoms. *Phys. Rev. Lett.*, 105:253001, 2010.
- [20] E.L. Raab; M. Prentiss; A. Cable; S. Chu; and D.E. Pritchard. Trapping of neutral sodium atoms with radiation pressure. *Phys. Rev. Lett.*, 59:2631, 1987.
- [21] N. Schlosser; G. Reymond; and P. Grangier. Collisional blockade in microscopic optical dipole traps. *Phys. Rev. Lett.*, 89:023005, 2002.
- [22] W. Rosenfeld. *Experiments with an entangled system of a single atom and a single photon*. PhD thesis, Ludwig-Maximilians-Universität München, 2008.
- [23] N. Ortegel. Atom-photon entanglement. Master's thesis, Ludwig-Maximilians-Universität München, 2009.
- [24] F. Henkel. *private communication*. 2011.
- [25] T.W. Hänsch and A.L. Schawlow. Cooling of gases by laser radiation. *Optics Communications*, 13:68, 1975.

- [26] J. E. Bjorkholm Alex Cable Steven Chu, L. Hollberg and A. Ashkin. Three-dimensional viscous confinement and cooling of atoms by resonance radiation pressure. *Phys. Rev. Lett.*, 55:48, 1985.
- [27] Steven Chu; J. E. Bjorkholm; A. Ashkin and A. Cable. Experimental observation of optically trapped atoms. *Phys. Rev. Lett.*, 57:314, 1986.
- [28] S. L. Rolston C. E. Tanner R. N. Watts P. D. Lett, W. D. Phillips and C. I. Westbrook. Optical molasses. *J. Opt. Soc. Am. B*, 6:2084, 1989.
- [29] H. J. Metcalf; P. van der Straten. *Laser cooling and trapping*. Springer Verlag, New York, 1999.
- [30] Christoph I. Westbrook Paul D. Lett, Richard N. Watts, Phillip L. Gould William D. Phillips, and Harold J. Metcalf. Observation of atoms laser cooled below the doppler limit. *Phys. Rev. Lett.*, 61:169, 1988.
- [31] J. Dalibard; C. Cohen-Tannoudji. Laser cooling below the doppler limit by polarization gradients: Simple theoretical models. *J. Opt. Soc. Am. B*, 6:2023, 1989.
- [32] Christopher J. Foot. *Atomic Physics*. Oxford University Press, New York, 2005.
- [33] Y. Ovchinnikov R. Grimm, M. Weidemüller. Optical dipole traps for neutral atoms. *arXiv:physics/9902072v1*, 1999.
- [34] L. Ricci; M. Weidemüller; T. Esslinger; A. Hemmerich; C. Zimmermann; V. Vuletic; W. König; T.W. Hänsch. A compact grating-stabilized diode laser system for atomic physics. *Optics Communications*, 117:541–549, 1995.
- [35] Daniel A. Steck. Rubidium 87 D line data. *available online at <http://steck.us.alkalidata> (revision 2.1, 1 September 2008)*.
- [36] Dan Maydan. Acoustooptical pulse modulators. *Journal of quantum electronics*, 6:15, 1970.
- [37] W. Rosenfeld. *private communication*. 2009.
- [38] A. Deeg. Zustandsdetektion eines einzelnen Atoms. Master’s thesis, Ludwig-Maximilians-Universität München, 2008.
- [39] B.E.A. Saleh; M.C. Teich. *Fundamentals of photonics*. Wiley, 2007.
- [40] J. Hofmann. *private communication*. 2009.

- [41] T. Bergeman; Gidon Erez; Harold J. Metcalf. Magnetostatic trapping fields for neutral atoms. *Phys. Rev. A*, 35:1535, 1987.
- [42] Todd Meyrath. Electromagnet design basics for cold atom experiments. Technical report, Atom Optics Laboratory Center for Nonlinear Dynamics, University of Texas at Austin, 2004.
- [43] David J. Griffiths. *Introduction to Electrodynamics*. Prentice-Hall, New Jersey, 1999.

Acknowledgments

I would like to express my thankfulness to those people who had helped me finish this work and accompanied me through this period of time. Without them the accomplishment of this work will not be possible.

- Professor Harald Weinfurter for giving me the opportunity to work in the group and creating such a friendly and enjoyable working environment.
- Markus Weber and Wenjamin Rosenfeld for their valuable advices helping me get through all kinds of difficulties while carrying out the work. Special thanks have to be attributed to Wenjamin for spending so much time on correcting my immature thesis writing and invaluable suggestions to make it better.
- Norbert Ortegel for advising and working together with me during the entire period. I learned a lot from the ingenious ideas he proposed for the experimental construction. Without his help on the software problems and correcting the first draft, it will be impossible for me to finish the thesis in such a short time.
- Michael Krug and Julian Hofmann for answering all the questions that I posed to them. This might be nothing for them, however, I benefit a lot. Special thanks to Julian for the CAD drawing of the MOT and letting me use the pictures of them. The soundtrack from Michael is simply awesome.
- Florian Henkel and Daniel Schlenk for their thoughtful advices on all kinds of things. It is always a pleasure for me to discuss about cultural and interesting stuffs with them.
- All the people in the xqp group for sharing such a nice atmosphere. In particular, Lea, Daniel, Lars, Johannes and Toshi, whom I always enjoyed chatting with while walking to the mensa everyday. Guys from Garching, Alex, Yvo, Christian and Daniel for many times of joyful beer drinking events.
- The wonderful girl Jore for her companionship. Her patient listening releases me from frustrations.
- My parents for everything. Without all the financial and mental supports from them, this two-year abroad study is simply impossible.